nature communications

Article

https://doi.org/10.1038/s41467-025-60181-x

Bioadhesive hydrogel-coupled and miniaturized ultrasound transducer system for long-term, wearable neuromodulation

Received: 23 July 2024

Accepted: 16 May 2025

Published online: 28 May 2025

Check for updates

Kai Wing Kevin Tang[1,4], Jinmo Jeong[1,4], Ju-Chun Hsieh[1,4], Mengmeng Yao[1], Hong Ding[1], Wenliang Wang[1], Xiangping Liu[1], Ilya Pyatnitskiy[1], Weilong He[1], William D. Moscoso-Barrera[1], Anakaren Romero Lozano[1], Brinkley Artman[1], Heeyong Huh[2], Preston S. Wilson[3] & Huiliang Wang[1]

Transcranial focused ultrasound is a promising non-invasive method for neuromodulation, particularly for neurodegenerative and psychiatric conditions. However, its use in wearable systems has been limited due to bulky devices and reliance on ultrasound gel, which dehydrates and lacks stable adhesion for long-term use. Here, we present a miniaturized wearable ultrasound device, comparable in size to standard electrophysiological electrodes, integrated with a bioadhesive hydrogel for stable, long-term somatosensory cortical stimulation. Our air-cavity Fresnel lens based self-focusing acoustic transducer was fabricated via a lithography-free microfabrication process, achieving 30.7 W/cm² (1.92 MPa) acoustic intensity and 10 mm focal depth. The hydrogel couplant exhibited less than 13% acoustic attenuation and maintained a stable adhesion force of 0.961 N/cm for 35 days. Using this system, we successfully suppressed somatosensory evoked potentials elicited by functional electrical stimulation over 28 days, demonstrating the device's potential for long-term, wearable neuromodulation applications.

The increase in brain diseases amongst the general population has motivated significant research in therapeutic treatment approaches. With 1 million people in the US diagnosed with Parkinson's disease and a projected increase of 78% annually, the socioeconomic burden on individuals, families, and the healthcare system is significant[1,2]. Deep brain stimulation (DBS) has been clinically approved in treating Parkinson's disease[3–7], essential tremor[8–12], epilepsy[13–16], dystonia[17–19], and obsessive-compulsive disorder[4,20]. Despite being a very effective method, it requires invasive implanted electrodes with complications involving hematoma, lead fractures, and glial response rendering electrodes ineffective[21,22]. Alternatively, non-invasive brain stimulation devices provide a unique opportunity for treatments in a multitude of psychiatric, mental, and neurodegenerative diseases in a substantial number of patients as a non-invasive intervention. Transcranial magnetic stimulation (TMS) are currently effective and clinically approved treatment methods for mental health disorders such as obsessive-compulsive disorders and depression[23]. It has also shown promising improvements in sleep disorders, Parkinson's[24], Alzheimer's[25], and potentially several other neuropsychiatric disorders[26]. However, TMS stimulates large brain areas due to its low spatial resolution, making it difficult to achieve the most effective treatment without causing adverse off-targeting effects[27–30]. Since TMS generally requires a 3–6 weeks treatment period and DBS require continuous stimulation upon implantation, there is a strong

[1]Department of Biomedical Engineering, Cockrell School of Engineering, The University of Texas at Austin, Austin, TX, USA. [2]Department of Aerospace Engineering and Engineering Mechanics, Cockrell School of Engineering, The University of Texas at Austin, Austin, TX, USA. [3]Walker Department of Mechanical Engineering, Cockrell School of Engineering, The University of Texas at Austin, Austin, TX, USA. [4]These authors contributed equally: Kai Wing Kevin Tang, Jinmo Jeong, Ju-Chun Hsieh. e-mail: evanwang@utexas.edu

need for non-invasive and high-spatial resolution neuromodulation approach with long-term wearability[6,25,31–33].

Transcranial focused ultrasound (tFUS) provides an alternative non-invasive strategy for highly precise targeting of subcortical and DBS with high spatial-temporal resolution[34]. It has shown improvement in neurological diseases such as tremor associated with Parkinson's disease[35,36], cognitive and memory impairments in Alzheimer's disease[37–41], epilepsy[42–44], and chronic mental health disorders[45]. However, the current tFUS systems are typically bulky and are not in wearable format for long-term neuromodulation. To develop an effective wearable ultrasound neuromodulation system requires: (1) miniaturized transducer with effective acoustic intensity and focality for tFUS[46], (2) stable fixation to the skin during neuromodulation[47], and (3) acoustic impedance match between the ultrasound transducer and tissue[48]. Currently, the commercial ultrasound gel has been commonly used as a medium to match the acoustic impedance during ultrasound stimulation by eliminating air gaps in promoting the efficiency of ultrasound transmission[49]. Yet, its limitations of non-adhesive properties for ultrasound transducer fixation to the skin and dehydration susceptibility prevents long-term use in continuous neuromodulation treatment of brain disorders over several weeks[50]. Current approaches in developing bioadhesive hydrogel for wearable ultrasound imaging application has shown to be effective for ultrasound applications, however, its efficacy diminishes drastically after 72 h[51,52]. Therefore, a wearable ultrasound device integrated with an acoustically compatible medium that provides robust device-to-skin adhesion for long-term application is desired.

In this work, we developed a strategy to address the current limitations of ultrasound devices to enable long-term cortical neuromodulation. Specifically, we have developed self-focusing acoustic transducers (SFAT) that leverages geometrical patterning of acoustic lens in altering wave propagation to achieve acoustic focusing through the use of air-cavity fresnel acoustic lens (ACFAL), allowing an increase in acoustic intensity of the focal depth limit originally constrained by the geometrical diameter of the transducer (Fig. 1a–c)[53]. In addition, we have designed bioadhesive hydrogel, consisting of 2-acrylamido-2-methyl-1-propanesulfonic acid (AMPS) and glycerol, to have high water absorption and rehydration properties over a month and strong adhesion to the skin (Fig. 1d). Through integration of bioadhesive hydrogel to our SFAT transducer, our **Min**iaturized and B**io**adhesive-coupled **Ul**trasound **Tra**nsducer (MiniUlTra) weighs 8.5 grams and can be easily attached to the target skin for an extended period, allowing ease of use for long-term applications (Fig. 1e–h). We evaluated the efficacy of MiniUlTra in its effectiveness in suppressing somatosensory evoked potential elicited by median nerve stimulation via functional electrical stimulation over 28 days, demonstrating MiniUlTra's efficacy in long-term cortical neuromodulation as a wearable ultrasound device.

Results

Development and characterization of miniaturized ultrasound transducer

Acoustic frequencies used for ultrasound stimulation with ideal transcranial transmission and brain absorption has been reported to be less than 650 kHz[54,55], where clinical demonstration of using ultrasound stimulation at 210 kHz and 500 kHz frequency in humans has shown effective suppression evoked potential and enhanced sensory functions[56,57]. Here, we used 650 kHz based on previous observations and studies demonstrating effective neuromodulation with improved spatial focality under the constraint of a miniaturized single-element transducer. Thus, we developed a custom miniaturized 650 kHz ultrasound transducer (similar size to standard electroencephalographic (EEG) electrode leads, OD = 18 mm) with microfabrication techniques to create a self-focusing acoustic transducer (SFAT) using ACFAL coupled with a highly adhesive and conformable bioadhesive hydrogel for long-term applications. Characterization of acoustic pressure fields emitted from our SFAT-ACFAL was done using a calibrated hydrophone (Fig. 2a) on a motorized 3-axis system submerged in a degassed distilled water bath. Comparison of acoustic field distribution with and without the ACFAL formed by PDMS (Pristine PZT vs. SFAT-ACFAL) showed less scattering and higher focusing on the desired focal point in the transducer with ACFAL (Fig. 2b). Recording of acoustic waveforms pulsed and transmitted was performed in free-field and with a human skull, where measurements indicate a spatial focality of 3.5 mm axially and 8 mm laterally (Fig. 2c, d). The focal depth was measured to be at 10 mm, at the expected and designed specification. To determine the acoustic intensity and biosafety of the devices for ultrasound neuromodulation, a calibration curve was performed with our ultrasound system (Image Guided Therapy System) used to drive the SFAT-ACFAL to evaluate the linearity of acoustic intensity and pressure when driving amplitude was increased. The measurements revealed a spatial-peak pulse-average intensity (I_{SPPA}) in the free-field to be less than 30.7 W/cm^2 (1.92 MPa) (Fig. 2e). To validate efficacious acoustic transmission of the device, initial peak pressure of SFAT-ACFAL measured in free-field with and without the human skull (~ 8 mm thick) resulted in a decrease from 1.37 MPa to 0.48 MPa corresponding to 64.8% decrease (3.81 dB, Supplementary Fig. 1), which is higher than the attenuation reported in macaque skull at frequency ranges 300–800 kHz (0.85–2.06 dB)[58], but less than that of in human skull (5.21–11.29 dB) with thickness at parietal section (~ 5.8 mm)[59]. To compare, a study has demonstrated free-field acoustic intensity of 23.9 W/cm^2 has shown to be effective when transmitting through the human skull with a four-fold drop in intensity to 5.9 W/cm^2[56]. Contrarily, through the human skull, the SFAT-ACFAL demonstrated an approximately six-fold drop in intensity (30.2 W/cm^2 to 3.92 W/cm^2) with an 8 mm thick skull in comparison to 5.8 mm. As such, all stimulation paradigms performed in healthy volunteers using our device were performed at 23.1 W/cm^2 (1.66 MPa), to necessitate sufficient acoustic intensity threshold in suppression of sensory evoked potentials[56]. The effect of transcranial skull transmission effectively attenuates the amplitude of the acoustic pulse waveform (Fig. 2f) and increases the spatial resolution resulting in a smaller focal spot. This is possibly due to the inhomogeneity of skull and tissue interfaced between the boundary conditions resulting in time-reversible wave propagation, commonly used for imaging[60]. The shift in axial peak of the focal spot (Fig. 2d) was due to the curvature of the human skull and its' difficulty in positioning between the hydrophone and device to prevent collision.

To ensure thermal biosafety, the device during ultrasound stimulation should not exceed an increase of 2 °C[61]. We then characterized the thermal biosafety of the device by performing the stimulation paradigm used by Legon et al. [56]. In comparison with higher duty cycle and pulse duration through the human skull and monitoring the temperature of the stimulation site using an infrared camera (Fig. 2g and Supplementary Figs. 2 and 3). Results indicated that with 10 min of continuous stimulation, the paradigm of 360 μs ON and 640 μs OFF[56] had a thermal increase less than 2 °C within 3 min. Similarly, when the duty cycle was increased to 50% (500 μs ON and 500 μs OFF) there was no significant temperature increase within 3 min. However, when the pulse duration increased to 100 μs ON and 900 μs OFF, change in temperature was negligible within 10 min. As the trials perform in this study is within 2 min, thermal safety was adhered to FDA guidelines (Fig. 2g). This demonstrates the device's safety regime for human applications. Electrical characterization of the device was performed using an impedance spectrum analyzer to determine the impedance and phase response of SFAT-ACFAL. The impedance was then used to determine harmonic frequencies where the lowest impedance (~ 174 Ω) represents the center frequency (~ 653 kHz) of choice used in designing of SFAT-ACFAL and

https://doi.org/10.1038/s41467-025-60181-x

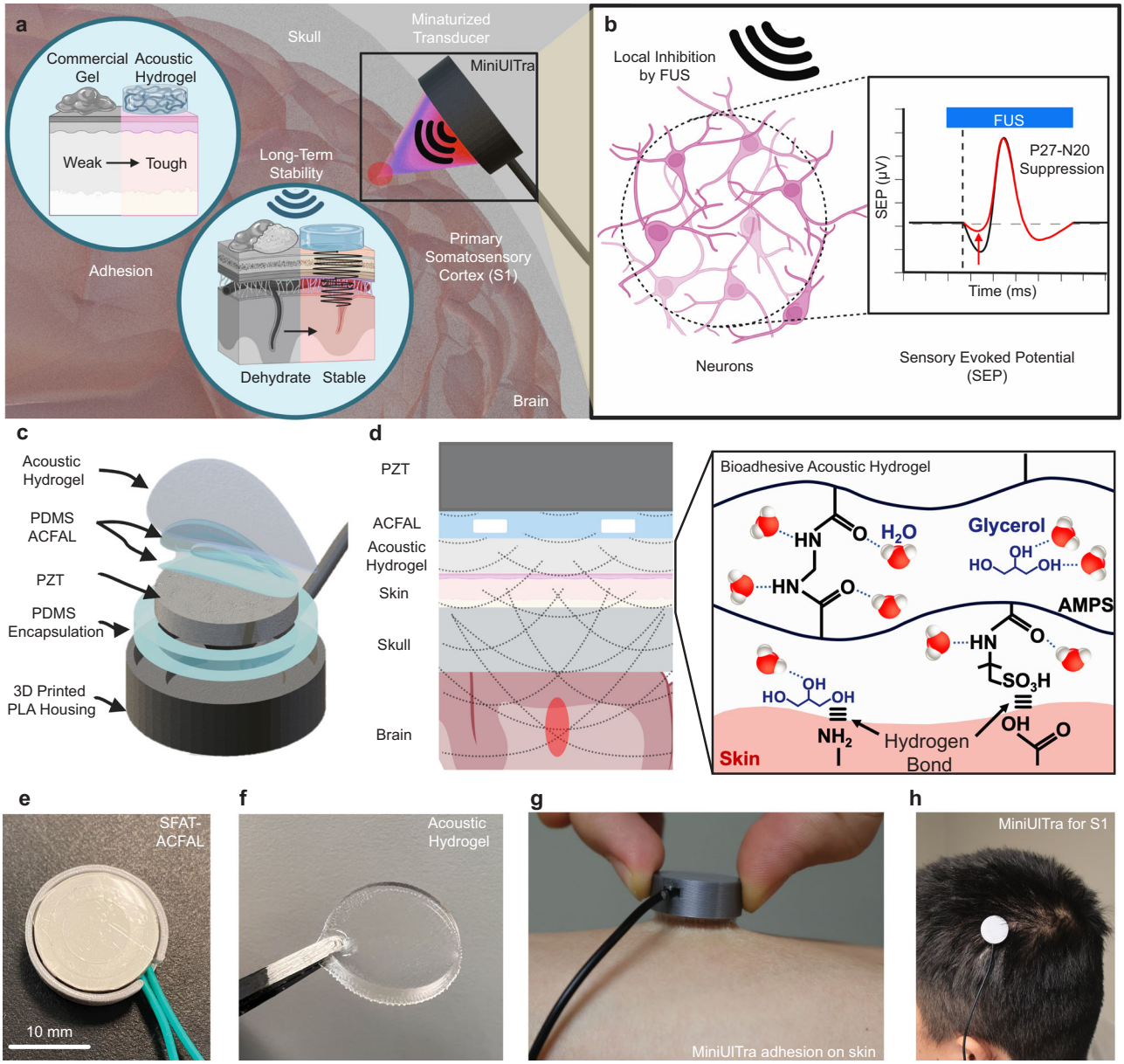

Fig. 1 | Miniaturized and bioadhesive-coupled ultrasound transducer (MiniUlTra). a Illustration of MiniUlTra that continuously adheres to the scalp targeting the primary somatosensory cortex (S1) with high adhesion force, low acoustic attenuation and miniaturized transducer. **b** Mechanism of suppression of P27-N20 complex in somatosensory evoked potential (SEP) through focused ultrasound stimulation locally at the S1. **c** Schematic of layered structure of MiniUlTra that assembles the piezoelectric with PDMS-based ACFAL and bioadhesive hydrogel integrated into a compact 3D-printed housing. **d** Side-view of layered schematic including chemical structure of bioadhesive hydrogel and its' adhesion mechanisms. **e**, **f** Optical images of design and fabricated SFAT-ACFAL and bioadhesive hydrogel. **g** Adhesion of MiniUlTra on skin. **h** Demonstration of MiniUlTra on the scalp for S1 targeted neuromodulation. Created in BioRender. Tang, K. (2025) https://BioRender.com/6fzf8qz.

also for impedance matching purposes[62] (Fig. 2h). Given the multiple resonances in impedance spectrum is present, further optimization is required. As a result, potential surface heating of the transducer may induce further thermal biosafety concerns. Thus, additional performance details of SFAT-ACFAL surface thermal profile were measured from 5 points on the surface for 120 s (1 pulse/sec) without commercial gel, with commercial gel, and with our bioadhesive hydrogel (Supplementary Fig. 3). Results demonstrate an overall increase of less than ~7 °C across all conditions and no more than 43 °C, where burn and necrosis in subcutaneous tissues begin to occur under FDA guidelines beyond 43 °C[63]. Furthermore, the skin and skull dissipate the heat as demonstrated through thermal heating measurement of MiniUlTra (Fig. 2g).

Development and characterization of bioadhesive hydrogel

To ensure long-term neuromodulation viability, the need for an acoustic couplant to sustain stable acoustic properties over time is needed to be integrated with the SFAT-ACFAL. Specifically, it should sustain hydration, effectively transmit ultrasound, adhere conformally to the skin with a low modulus to minimize air gaps, and maintain high adhesion force over time[51,52]. The bioadhesive hydrogel used in this study includes two primary materials: (1) 2-acrylamido-2-methylpropane sulfonic acid (AMPS) and (2) glycerol (Fig. 1d). PolyAMPS is an ionic polymer with a hydrophilic sulfonic group resulting in it being inherently negatively charged, which allows for strong ionic interaction with water molecules[64]. Thus, it enables a high water absorption rate[65–67], allowing for a sustained hydrated state through the absorption of ambient

https://doi.org/10.1038/s41467-025-60181-x

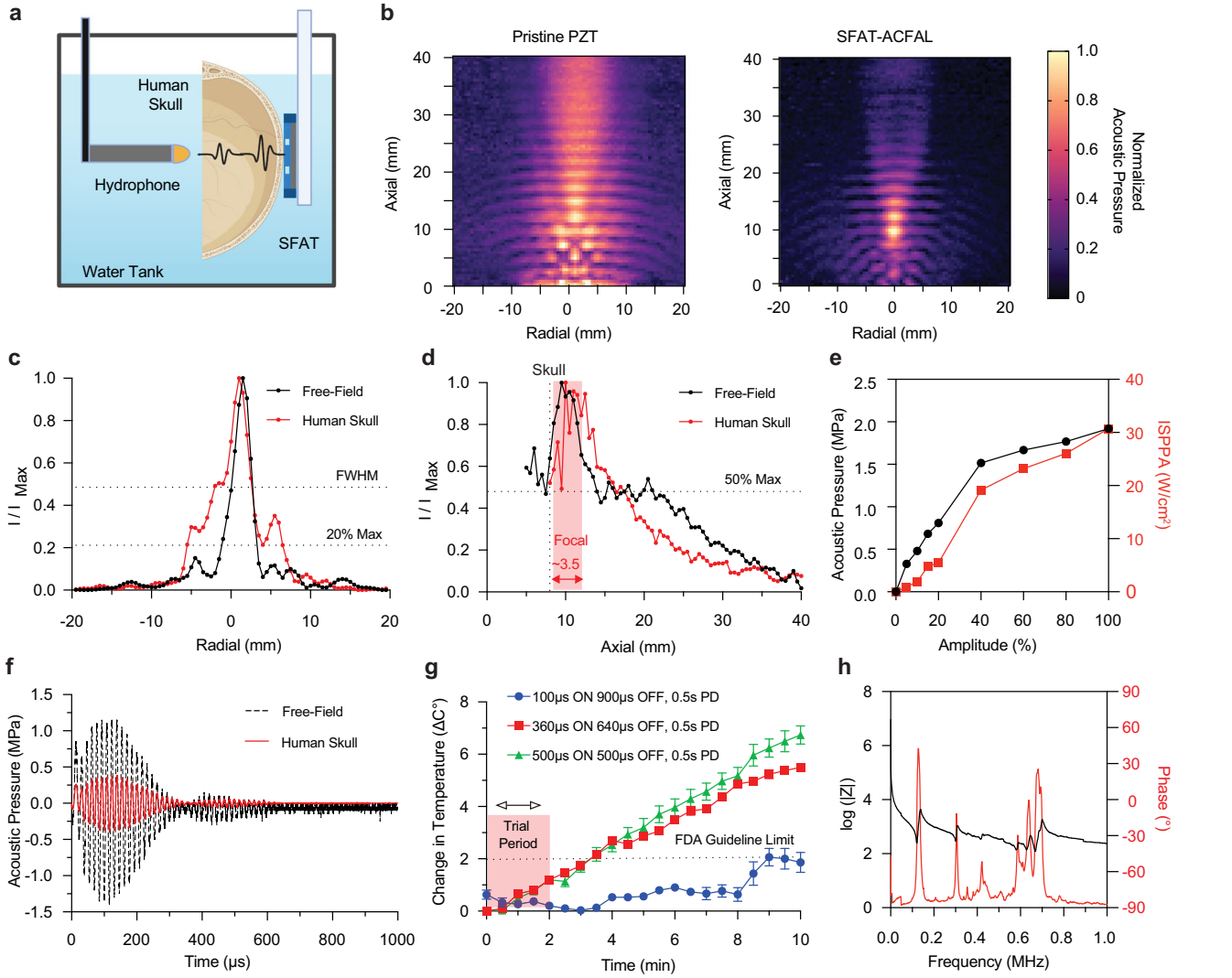

Fig. 2 | Self-focusing acoustic transducer (SFAT) using air-cavity Fresnel lens (ACFAL). a Schematic of experimental setup for characterization of SFAT-ACFAL. **b** Comparison of acoustic field distribution and intensity with Pristine PZT (left) and with PDMS-based ACFAL (right) in free-field water. **c** Normalized radial acoustic intensity profile in free-field and with the presence of a human skull at focal depth 10 mm. **d** Normalized uniaxial acoustic intensity profile in free-field and with the presence of a human skull. **e** Acoustic pressure (MPa) and intensity (I_{SPPA}) calibration curve measured when SFAT-ACFAL at varying driving amplitude using ultrasound generator system. **f** Measured waveform of ultrasound pulse using stimulation paradigm of 360 μs with and without human skull. **g** Thermal effect of SFAT-AFAL on human skull measured with infrared camera on varying stimulation parameters (mean ± s.e.m., $n = 3$, independent experiments). **h** Electrical impedance and phase of SFAT-ACFAL. All data generated in this figure are provided in the Source Data file. Created in BioRender. Tang, K. (2025) https://BioRender.com/6fzf8qz.

moisture[68]. In addition to its high water content and retention, Poly-AMPS provides modulus similar to that of biological tissues[69], and is suitable as a long-term substitute of commercially available ultrasound gel that tends to dehydrate within hours. Furthermore, the addition of glycerol containing hydroxyl groups, which forms hydrogen bonds with water molecules, provides water retention capacity and enhanced adhesion to the skin by offering a hydrating effect on the stratum corneum[65,70,71].

We characterized the acoustic attenuation rate of our bioadhesive hydrogel at different thickness in comparison to commercial gel. As a result, we observe that the ultrasound power attenuation of the bioadhesive hydrogel is comparable to that of commercial gel at thicknesses of 0.5 mm and 1 mm (Fig. 3a). With ultrasound as a mechanical acoustic wave, the mismatch in impedance when propagated between mediums with varying acoustic impedances inevitably leads to partial transmission and reflection at the boundary layers. By minimizing the mismatch in impedance, reduction of reflected and maximizing transmitted waves provides higher acoustic intensity deposition to the target site. Therefore, the need for minimizing the impedance mismatch between our device and the skin using our bioadhesive hydrogel is necessary[51]. As acoustic speed in a material is directly related to its elastic properties and density, the acoustic impedance could be derived directly from the acoustic speed and density[72,73]. We experimentally characterize and measure the acoustic speed of our hydrogel. Firstly, with the acoustic speed of water being 1500 m/s and the distance between PZT and hydrophone positioned 20 mm apart in the water tank, the time required for an acoustic pulse (time-of-flight, ToF) to travel from the transducer to the hydrogel theoretically will be 13.3 μs in free-field. Upon measurement of ToF with the hydrogel, comparison of to the free-field measurement allows us to determine the time difference and the acoustic speed through the hydrogel (Fig. 3b). With the measured density of the hydrogel being 1166.7 kg/m^3, the derived acoustic impedance of the hydrogel yielded 2.13 ± 0.11 MRayl and 2.17 ± 0.13 MRayl, with estimated acoustic

https://doi.org/10.1038/s41467-025-60181-x

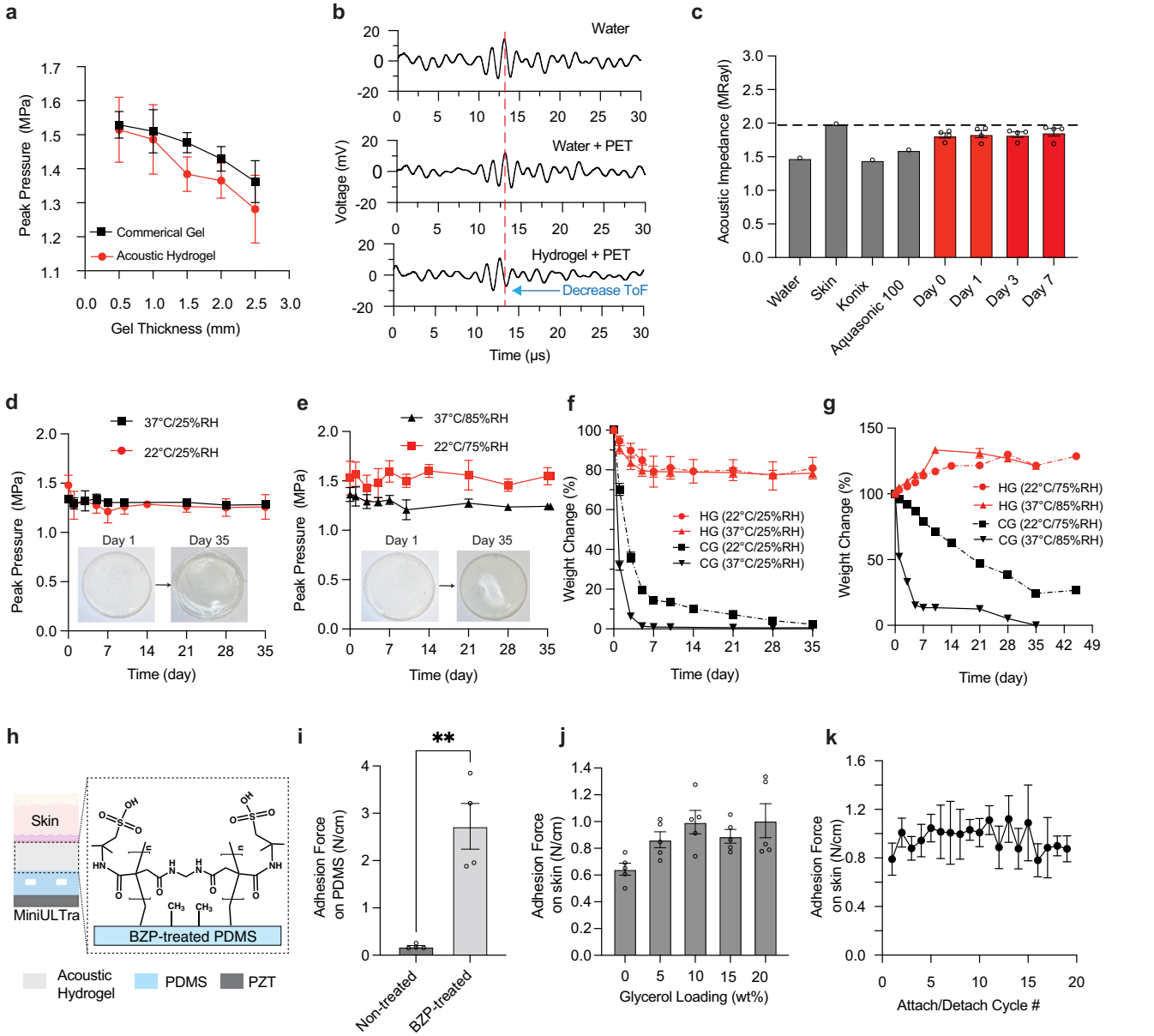

Fig. 3 | Bioadhesive hydrogel. a Comparison of ultrasound intensity decreases according to thickness changes in bioadhesive hydrogel and commercial gel (Aquasonic 100, Parker), ($n = 6$, independent samples for each thickness). **b** Comparison of acoustic time-of-flight (ToF) for ultrasound transmission through water, PET, and hydrogel. **c** Acoustic impedance of the hydrogel for 7 days ($n = 4$, independent samples each day) compared to commercial gel, water, and human skin. **d** Peak-pressure attenuation of bioadhesive hydrogel under 22 °C/25% humidity (red line) and 37 °C/25% humidity (black line) over 35 days ($n = 4$, independent samples). **e** Peak-pressure attenuation of bioadhesive hydrogel under 22 °C/75% humidity (red line) and 37 °C/85% humidity (black line) over 35 days ($n = 4$, independent samples). **f** Weight change of the bioadhesive hydrogel and commercial gel under 22 °C/25% humidity (CG Commercial Gel, HG Bioadhesive hydrogel, $n = 4$, independent samples). **g** Weight change of the bioadhesive hydrogel and commercial gel under 22 °C/75% humidity (solid line) and 37 °C/85% humidity (dashed line) conditions (CG Commercial Gel, HG Bioadhesive hydrogel, $n = 4$, independent samples). **h** Chemical structure of the bioadhesive hydrogel integrated ACFAL by grafting the bioadhesive hydrogel to benzophenone (BZP) treated PDMS. **i** Improvement of adhesion force with BZP-treated PDMS ($n = 4$, independent samples, Two-sided unpaired t-test). **j** Adhesion force of the bioadhesive hydrogel according to glycerol loading change ($n = 5$, independent samples). **k** Adhesion force of the 20-cycle attachment/detachment test of the bioadhesive hydrogel on skin ($n = 4$, independent samples). All plots show mean ± s.e.m unless otherwise mentioned, $^{*}P < 0.05$, $^{**}P < 0.01$, and $^{***}P < 0.001$. All data generated in this figure are provided in the Source Data file. Created in BioRender. Tang, K. (2025) https://BioRender.com/6fzf8qz.

speed of 1816 ± 76.36 m/s and 1864 ± 113.7 m/s on day 0 and day 7, respectively (Fig. 3c and Supplementary Fig. 4). Overall, the acoustic impedance of the bioadhesive hydrogel remained stable across 7 days, with an average hydrogel impedance of 2.17 MRayl. Compared to the acoustic impedance of 1.99 MRayl for skin[52], our bioadhesive hydrogel exhibits a much more similar impedance to human skin[74–77], indicating minimum acoustic loss of our hydrogel in addition to its' long-term stability with minimal mismatch between the hydrogel and skin (1.99 MRayl) when evaluating acoustic transmission efficiency. Results show an overall higher transmission and reduced reflection coefficient when compared to commercial gels (Konix: 1.45 MRayl, Aquasonic 100: 1.60 MRayl), water, and skin[48,51,78,79] (Supplementary Fig. 4). Therefore, indicating minimum acoustic loss of our hydrogel in addition to its' long-term stability.

The water retention capacity of bioadhesive hydrogels as a function of AMPS ratio for long-term neuromodulation applications was

investigated. We prepared bioadhesive hydrogels with 24.4, 32.3, 38.9, and 44.3 w/w% of AMPS ratio, respectively. The swelling ratios ($weight_{time\ submerged\ in\ water}/weight_{initial}$) of the hydrogels (with 24.4, 32.3, 38.9, and 44.3 w/w% AMPS ratio) after 3 h were 7690%, 5750%, 4860%, and 4450%, respectively, where the hydrogel with the lowest AMPS ratio showing the highest swelling ratio due to the large pore size of hydrogels with crosslink ratio resulting increased swelling ratio (Supplementary Fig. 5A)[80]. To evaluate the dehydration and rehydration characteristics of the hydrogels as an effect of the AMPS amount in the air condition, the hydrogels for each AMPS ratio were stored at 37 °C degrees at low humidity (RH 25%) for the first three days and at high humidity (RH 85%) for the next three days, thus showing the dehydration and rehydration characteristics of the hydrogels. During the first three days at low humidity, the hydrogels exhibited dehydration rates of 69.9%, 79.0%, 82.5%, and 83.3%, with the hydrogel containing the lowest AMPS ratio dehydrated more. In the high humidity phase from days 3 to 6, rehydration ratios for the hydrogels were 156.6%, 151.4%, 150.5%, and 151.2%, indicating comparable water retention across different AMPS ratios, though those with lower AMPS ratios showed slightly higher rehydration. By day 6, the hydrogel with 24.4% AMPS had the lowest absolute weight, demonstrating higher dehydration and less stability than those with higher AMPS ratios (Supplementary Fig. 5B). The water retention ability of a hydrogel can be evaluated by comparing the dehydration rate of the hydrogel over time, and with a dehydration rate of 82.5% over 3 days, the water retention ability of our bioadhesive hydrogel (with 38.9 w/w% of AMPS) is comparable to other wearable hydrogel applications[81–83]. Overall, hydrogels with AMPS ratios of 32.3 w/w% or higher exhibited relatively lower dehydration and higher rehydration rates.

Further investigation of the long-term stability of the hydrogel in acoustic attenuation was performed under low and high humidity conditions at room and body temperatures. Low humidity of 25–30% mimicked a typical indoor room environment and 75–85% reflects high humidity outdoor conditions, which was emulated by a sealed humidity controlled container storage where the hydrogel was stored in a controlled temperature incubator[84,85]. Here, our hydrogel had an attenuation of up to ~9% and less than ~5% when stored in humidity conditions of ~25% and ~85%, respectively over 35 days (Fig. 3d, e). Additionally, weight change test was also performed for both our hydrogel and a commercial gel stored in these two humidity conditions (Supplementary Figs. 6 and 7). Under low humidity (~ 25%), our hydrogel exhibited a slow dehydration rate, retaining 79.6% of its weight and remained stable post 7 days. Conversely, the weight of the commercial gel decreased significantly with only 0.2% weight retention on day 7 (Fig. 3f), indicating that it was completely dried. Under high humidity (RH 75%), our hydrogel had a significant and consistent increase in weight of approximately 121% after 35 days (Fig. 3g). The only time the weight of the hydrogel in the high humidity condition increased to 133% in week 2 was because the humidity in the incubator increased from 85% to 95% at that time. It then stabilized again as the humidity was maintained at 85% later.

To ensure long-term robustness in wearability, sufficient adhesion between SFAT-ACFAL and the skin is necessary. Additionally, strong adhesion between the hydrogel and the PDMS-based ACFAL is required aside from the interface between hydrogel and the skin to prevent detachment. The robust integration between ACFAL and hydrogel was achieved by using the photografting agent for the hydrogel. Treating PDMS with benzophenone (BZP), a type II photoinitiator, extracts hydrogen from the grafted surface of PDMS and generates radicals allowing the PDMS and hydrogel to form a polymeric bond under UV irradiation[86] (Fig. 3h). As a result, the adhesion of BZP-treated PDMS to the hydrogel was 2.09 N/cm, which was 13 times higher than the adhesion of non-treated PDMS to the hydrogel (0.1513 N/cm) (Fig. 3i). Optimization of our hydrogel's adhesiveness to the skin was achieved by tuning the loading of glycerol and was determined via measurement of adhesion force through 90° T-Peel test. As the glycerol loading increases, the adhesion force of the hydrogel improves and plateaus when glycerol loading exceeds 10 wt% (Fig. 3j). In this study, glycerol was loaded at 20 wt% to maintain high water retention properties, allowing an adhesion force of ~0.941 N/cm, comparable with other wearable hydrogel applications and sufficient for attachment to the skin[87–89]. Skin adhesion cycling was performed subsequently to determine the adhesive reusability, where adhesion force remained stable over 20 cycles with a mean adhesion force of 0.961 N/cm (Fig. 3k). Modulus compliance of hydrogel with skin was investigated, where the modulus of the hydrogel is ~31.4 kPa, similar to that of skin tissues. As a result, the minimal mechanical mismatch demonstrates suitability of skin-device interface for long-term use (Supplementary Fig. 8)[90]. These results further indicate that the bioadhesive hydrogel could provide an alternative to long-term ultrasound applications.

SFAT-ACFAL enables suppression of somatosensory evoked potentials at S1 targeting

Studies in SEP by median nerve (MN) stimulation have been explored and researched greatly. Well-defined characteristic morphology of EEG signals of SEP are distinguished into waveform peaks assigned by their polarity (positive P or negative N) and its corresponding post-stimulus latency (in ms)[91]. The changes in latency and amplitudes of these waveform peaks are often interpreted as dynamical alterations in neural activity as a result of combination from peripheral and central nervous system to external stimulus. Specifically, early SEP peaks or "short latency" SEPs occurring within 40 ms post-stimuli are of great importance as they have the least variability in response to peripheral external stimulation whereas long latency responses are susceptible to cognitive factors and higher ordered complex neural processing of the sensory pathways[91]. Thus, waveform peaks of N20, P27, N33, P50, N70, P100, and N140 were examined. In brief, each of these peaks serve as a biomarker with implications of tactile information processing. However, of most great interest corresponds to N20 (or commonly known as P27-N20 complex) has been highly known for its relevance to the sensory input of dorsal column-medial lemniscal pathway and acts as a primary evoked response in response to peripheral stimuli to the lateral portion hand area of somatosensory cortex extended posteriorly over to supramarginal gyrus[92].

Recently, tFUS stimulation at the somatosensory cortex has been shown to suppress somatosensory evoked potential (SEP) via the elicitation of sensory stimuli. The suppression in SEP effectively resulted in higher subjects' ability to discriminate fine differences in two points through sensory perception at the epidermis of distal phalanges[56]. To demonstrate the efficacy of our SFAT-ACFAL, we applied our device in targeting the left S1 through transmission of tFUS into the cortex at the CP3 site (Fig. 4a). EEG electrodes using commercial Ag/AgCl was applied at the scalp of electrode sites CP1, C3, P3, and CP5 in the 10–20 EEG configuration as a means to study the influence of tFUS short-to-late onset evoked brain activity through understanding of changes in peak-to-peak amplitudes of SEP complexes and spectral changes in power elicited by the contralateral (right) MN stimulation with functional electrical stimulation (FES) (Fig. 4b).

To determine the efficacy in SEP suppression of our miniaturized transducer, we first applied commercially available ultrasound gel coupled between the SFAT-ACFAL with the scalp at the 10–20 EEG electrode site CP3. 650 kHz tFUS beams were pulsated to the target region ($n = 5$) with a pulse of 360 μs ON and 640 μs OFF at a pulse repetition frequency (PRF) of 1 kHz for 500 ms. The stimulation paradigm chosen has been demonstrated experimentally in humans to suppress SEP[56] whilst ensuring minimal thermal heating effects with our device due to the short pulse time (Fig. 2g). MN stimulation occurred for 200 μs at 100 ms after the beginning of tFUS transmission. Sham and tFUS treatment conditions were performed identically

https://doi.org/10.1038/s41467-025-60181-x

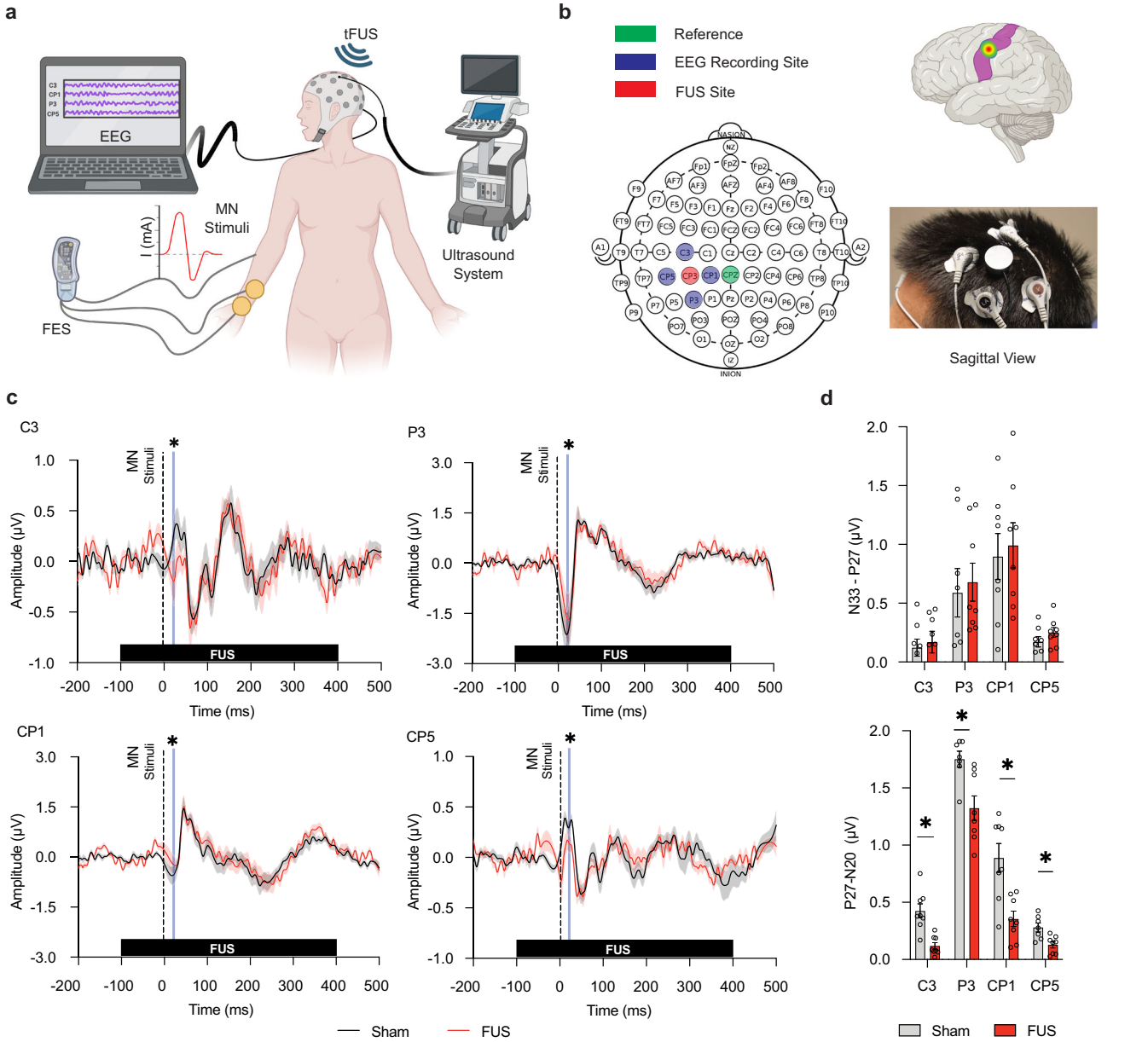

Fig. 4 | Evaluation of neuromodulation in somatosensory evoked potential using SFAT-ACFAL. a Schematic representation of experimental setup. **b** Illustration of EEG electrode and SFAT-ACFAL placement in 10–20 EEG montage with its corresponding targeting of left S1 with FUS at CP3. **c** Grand average of epochs where median nerve (MN) stimulation occurs at $t = 0$ ms and FUS or sham begins at $t = -100$ ms (red line indicates SEP under FUS+, black line indicates SEP under sham, highlighted blue indicates where significant difference was observed P27-N20 complex in SEP). **d** Summary of effect of FUS compared to sham in P27-N20 and N33-P27 complexes of SEP. Suppression of early onset P27-N20 complex observed across C3, P3, and CP5 in SEP by FUS ($n = 8$ per group, Two-sided Wilcoxon signed-rank test, 7 male and 1 female). All plots show mean ± s.e.m unless otherwise mentioned, $^{*}P < 0.05$, $^{**}P < 0.01$, and $^{***}P < 0.001$, $^{****}P < 0.0001$ (Supplementary Tables 1–4). All data generated in this figure are provided in the Supplementary Information/Source Data file. Created in BioRender. Tang, K. (2025) https://BioRender.com/6fzf8qz.

apart from the device being turned off in the sham group. Some subjects reported auditory chirping noises initially at the beginning of each trial produced by the device during stimulation. However, the chirping noises quickly subsided within a few seconds reported by subjects. Additionally, subjects did not report any discomfort, heating, or abnormal sensations at the site of tFUS treatment between sham and tFUS treatments.

With our device for tFUS treatment, we demonstrated a significant decrease in short latency peaks (P27-N20 complex) across electrode sites at C3 (sham, 0.425 ± 0.175 μV s.e.m.; tFUS 0.119 ± 0.082 μV s.e.m), P3 (sham, 1.752 ± 0.186 μV s.e.m.; tFUS 1.324 ± 0.301 μV s.e.m), CP1 (sham, 0.888 ± 0.355 μV s.e.m.; tFUS 0.355 ± 0.191 μV s.e.m), and CP5 (sham, 0.280 ± 0.103 μV s.e.m.; tFUS 0.128 ± 0.076 μV s.e.m) compared to the sham. tFUS using SFAT-ACFAL did not produce any significant changes in long-latency peaks (Fig. 4c, d and Supplementary Tables 1–4) but late potential (> 140 ms) showed general attenuation across all electrodes in late-onset SEP complexes.

Spectral decomposition of EEG signals enables understanding of spatial-temporal changes in dynamics regarding excitation and inhibition of cortex in response to information processing[93,94]. Therefore, spectral analysis was performed on the grand averaged epochs of SEP to evaluate the effects of tFUS using SFAT-ACFAL. By taking the difference between the spectral decomposition of FUS and sham, a significant short latency decrease in alpha (7–12 Hz) and beta (13–30 Hz)

https://doi.org/10.1038/s41467-025-60181-x

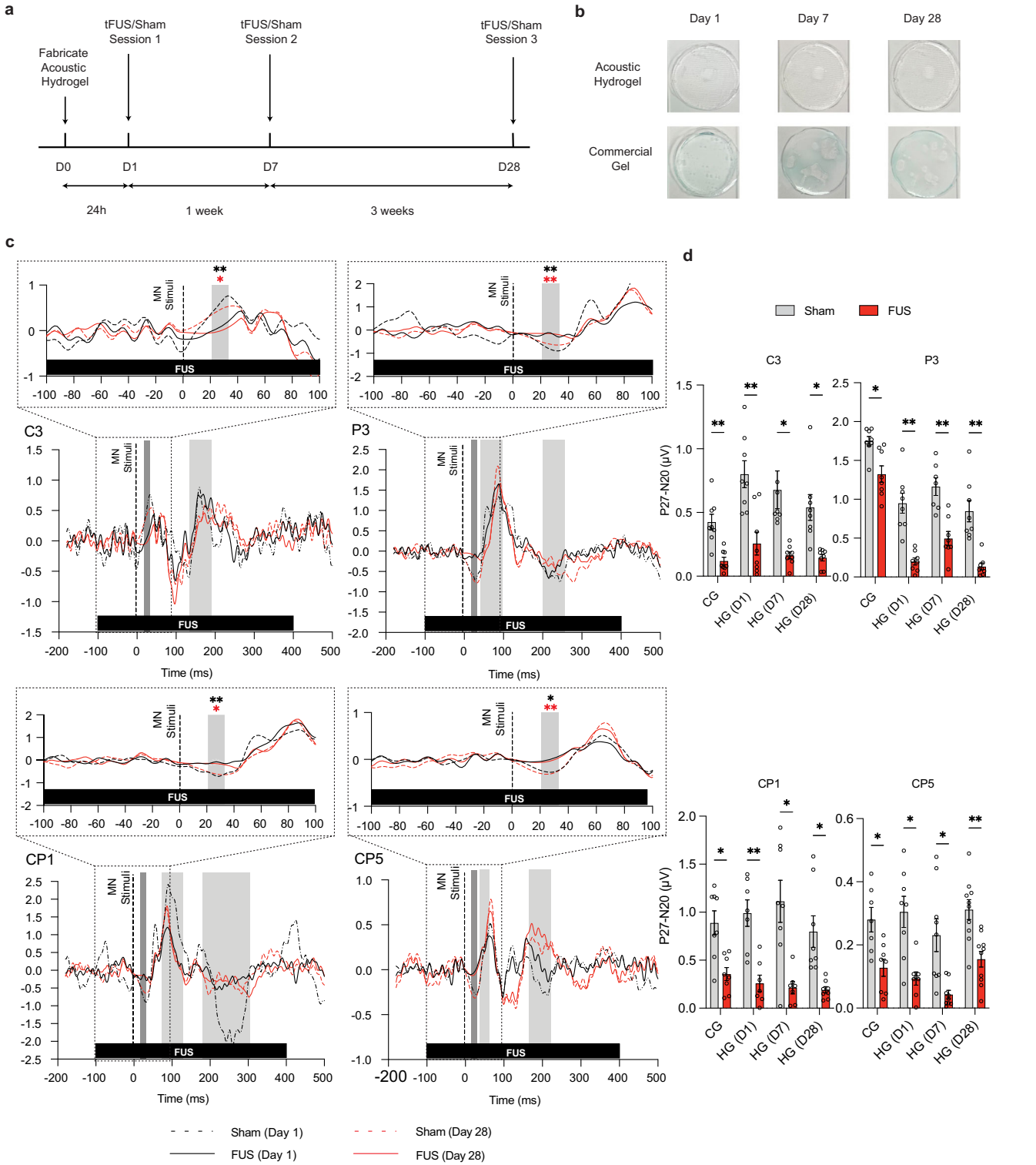

band power of −6 dB was observed within 100 ms of MN stimuli. Additionally, a short period of low gamma band (30–50 Hz) power decrease was observed around 100 ms post MN stimuli (Supplementary Fig. 9).

Long-term wearability and neuromodulation of MiniUlTra

The ability for our device to stimulate the S1 region long-term was tested within the same experimental protocols that target the characteristic pattern of SEP with MN stimuli. Particularly, SEP suppression via tFUS tests were conducted in 3 sessions (Days 1, 7, and 28) throughout 28 days (Fig. 5a) to investigate the efficacy of neuromodulation using our MiniUlTra device (bioadhesive hydrogel incorporated) on healthy volunteers ($n = 8$). The length of the experimental protocol was chosen to investigate the extreme longitudinal conditions of our MiniUlTra device over a month period, where our bioadhesive hydrogel remains stable compared to commercial gel over 28 days (Fig. 5b). To ensure tFUS did not generate noise, artifacts, or off-targeted evoked potentials, comparison of baseline (FUS−FES−) and stimulation (FUS + FES−) indicated no difference suggesting our device and FUS did not induce artifacts or off-targeted effects

Fig. 5 | Long-term suppression of the P27-N20 complex in somatosensory evoked-potential (SEP) using MiniUlTra. a Long-term experimental protocol for evaluating efficacy of hydrogel. The hydrogel was fabricated a day before the first session (D0). Three sessions per subject, each consisting of 10 trials of 3 min, each trial consisting of 120 epochs (tFUS/Sham) on day 1 (D1), 7 (D7), and 28 (D28). Each subject had their personal hydrogel with the device, which was stored in room temperature and ~30% humidity. **b** Optical image of prepared hydrogel compared to commercial ultrasound gel with the corresponding sessions. **c** Grand average epochs comparing effects of sham and FUS with median nerve (MN) stimulation on SEP across days 1, 7, and 28 using hydrogel. MN stimulation occurs at $t = 0$ ms and FUS or sham begins at $t = -100$ ms (black solid line indicates SEP under FUS+ on day 1; black dashed line indicates SEP under Sham on day 1; red solid line indicates SEP under FUS+ on day 28; red dashed line indicates SEP under Sham on day 28; highlighted dark gray indicates where significant difference was observed P27-N20 complex in SEP; highlighted light gray indicates where observable differences in long latency complexes). **d** Suppression of early onset P27-N20 complex observed across C3, P3, CP1, and CP5 in SEP by FUS shown within each group. No significant difference was observed across FUS groups in bioadhesive hydrogel (HG) when compared to the FUS group using commercial gel (CG). Significant decrease in P27-N20 complexes was observed when comparing within each day of the hydrogel. ($n = 8$ per group, Šídák multiple comparison One-way ANOVA, 8 male). All plots show mean ± s.e.m unless otherwise mentioned, $^{*}P < 0.05$, $^{**}P < 0.01$, and $^{***}P < 0.001$ (Supplementary Table 5). All data generated in this figure are provided in the Supplementary Information/Source Data file.

(Supplementary Fig. 10). When MiniUlTra was used on day 1, significant suppression of SEP was observed compared to the sham group across all electrode channels. Furthermore, there was no significant difference between the treatment group when our bioadhesive hydrogel was used compared to commercial gel, validating the acoustic characteristics of the bioadhesive hydrogel in ultrasound transmission has similar performance to commercially available ultrasound gel (Fig. 5c, d). Additional sessions were performed on day 7 and day 28, which also showed significant suppression against the sham condition across all channels except for CP1 on day 7. We also observe a significant decrease in the P27-N20 complex over time (Supplementary Table 5). Overall, the SEP amplitude across the epoch was observed with clear decreases in short (P27-N20 complex) and long latency (> 70 ms) biomarkers (Fig. 5c). However, long latency biomarkers are more complex in its relation with median nerve stimuli due to its association with indirect somatosensory pathways involving cognitive and motor processes[95]. Hence, the P27-N20 complex was focused due to its prominent and well established association to contralateral stimuli at the S1 region[96,97]. Results indicated significant reduction in amplitude at the corresponding P27-N20 complexes across all electrode channels over 28 days (Fig. 5d), demonstrating robustness in ultrasound neuromodulation over long time stimulation with our MiniUlTra.

Discussion

We have demonstrated and developed a bioadhesive hydrogel coupled and miniaturized wearable ultrasound transducer that offers long-term brain neuromodulation capability without the need of handheld operators and fixtures. The device utilizes an alternative simplified microfabrication approach without the need of standard lithography techniques for SFAT-ACFAL patterning to achieve higher focality, acoustic intensity, and miniaturization. Additionally, our development of a hydrogel provides mechanical compliance, bioadhesion and stable acoustic coupling between our device and skin interface. For the first time, our hydrogel has shown acoustic and adhesive stability for more than a month compared to current state-of-the-art bioadhesive hydrogel's stability of 72 h. By integrating the two components, our device MiniUlTra can be used to perform noninvasive focused ultrasound stimulation delivered into the cortical region over 28 days with robust performance and clinical applications. Biosafety of the device was demonstrated to achieve spatial pulsed averaged intensity and acoustic pressure within the safety limits suggested by FDA guidelines and literature. Thus, our system provides a promising platform for non-invasive long-term wearable ultrasound applications.

Targeting via neuro-navigation and other modalities can be difficult due to the variances in anatomical dimensions and structures across subjects. Furthermore, the cranial thickness variation can be even more crucial when considering tFUS. In the present study, we delivered tFUS beams to the S1 using 10–20 EEG montage for navigation as our approach for targeting. The projection of the measured acoustic field beam alongside our targeting method was consistent with the physiological response of tFUS in suppression of SEP specifically for the P27-N20 complex. The validity of tFUS targeting via SEP amplitude change has been demonstrated whereby off-targeting of the S1 Brodmann areas 3B/1 of 1 cm posterior and anterior resulted in diminished effects of SEP suppression of tFUS elicited by MN stimulation[56]. It should be noted that MiniUlTra's focal resolution of 10 mm in depth and ~8 mm width covers a large section of the S1 provided within 1 cm of off-targeting.

To evaluate whether if FUS was successful in suppressing SEP, it is important to determine whether FUS alone (FUS+/FES−) would generate any evoked potentials, where it has been in other works that FUS elicited auditory and visual evoked potentials at the auditory and visual cortex, respectively[57,98]. As such, FUS alone was compared to baseline epochs (FUS+/FES− vs. FUS−/FES−) and but not elicitation of FUS evoked-potentials was observed (Supplementary Fig. 10). However, slight changes in amplitude were observed in P3 and C3 channels, which may align with results previously demonstrating FUS-evoked potential in somatosensory evoked potential[99]. Whilst results are unclear given the difference in stimulatory paradigms, further works on evaluation of the elicitation of FUS-evoked potential using MiniUlTra can be investigated to provide greater validation on the targeting methods.

All tFUS stimulation parameters used on the S1 cortex located at CP3 through 10–20 montage localization were maintained in brief exposures (3 min per trial, 120 pulses per trial, 360 μs ON 640 μs OFF, 0.5 ms pulse duration, 1 Hz PRF), with total duty cycle of each trial at 36%. This led to negligible measured temperature increase (< 0.2 °C) at the base of a human skull where the S1 cortex is expected (Supplementary Figs. 2 and 3). Additionally, the mechanical index (MI) measured in-vitro at the targeted brain area ($f = 10$ mm) through the human skull was less than 0.125, lower than the FDA guideline (< 1.9). The low MI suggests unlikely brain tissue cavitation for neuromodulation[100,101].

In this work, the acoustic characterization of SFAT-ACFAL used in MiniUlTra were performed with a fragment of the parietal section of a human skull. Whilst tFUS offers high spatial resolution compared to other non-invasive techniques, the presence of other factors involving standing waves, diffraction and resonance due to the enclosed structure of a realistic human skull was not taken into consideration[58]. In particular, the inhomogeneity structure of the skull both geometrically and composition can result in off-targeting and unintended beam structures when targeting the S1 region resulting in ineffective or unintended stimulatory effects. Thus, why we performed axial and radial acoustic field characterization of our device with the human skull and resulted in a broader full-width half maximum and shifted focal depth (Fig. 2c, d). Ideally, conducting volumetric pressure mapping from the base of human skull like that of Fig. 2b would provide greater insight on the effects of acoustic transmission. However, due to the geometrical curvature of the skull and the need to prevent collision of the hydrophone with the skull, we opted to perform 1-D measurement for in-vitro characterization.

Caution should be taken when considering the efficacy of MiniUlTra's wearability in the general population. Our major constraint was due to the difficulty in high volume hairstyles, which made it difficult to

identify and access the scalp for CP3 when placing the MiniUlTra. Regardless of how adhesive our hydrogel may be, unlike conductive EEG gel used for recording, complete unimpeded contact between the device and the scalp is crucial to necessitate effective acoustic transmission. The presence of any hair fiber will introduce greater acoustic impedance and diffraction of waves resulting in ineffective tFUS. As such, subjects recruited were primarily with low hair volume. Here, we carefully brush aside the hair to ensure good contact with the scalp at CP3 with our device. Through this, we were able to obtain successful SEP suppression consistent with other works in using tFUS for evoked potential suppression.

A potential confounding factor to the above experiments was the lack of randomization of tFUS and sham ultrasound conditions across subjects. Specifically, all subjects received the same combination of stimuli groups (FUS−FES−, FUS−FES+, FUS+FES−, FUS+FES+) without knowing the specific sequence or order as a form of single-blinded approach to help mitigate placebo and bias. However, the thermal heating and mechanical vibration of the transducer may potentially remove the single-blinded nature of FUS conditions by subjects (Supplementary Fig. 3). As such, post-ad hoc analysis of questionnaire given to subjects indicated self-report of **5 out of 8** subjects were unaware when they were receiving FUS− or FUS+ conditions (Supplementary Fig. 11) despite reporting that they were able to perceive tingling sensations during these trials.

Regarding the number of electrode channels for recording SEP, source localization using high-density EEG recordings and analysis offers high spatial-temporal resolution, enabling observation of detailed effects of SEP based on tFUS targeting[102–105]. However, many prior studies assessing tFUS effects on visual evoked potentials (VEP)[98,99] and sensory evoked potentials (SEP)[56,106] employed 2–4 EEG electrodes positioned in corresponding cortical regions using the 10–20 electrode montage. In these studies, electrode placement and tFUS targeting were determined by the international 10–20 EEG system, and placement accuracy was validated through VEP and SEP spikes observed in EEG recordings. For example, the comparison between sham (FUS−FES+) and stimulation (FUS+FES+) conditions confirms successful SEP elicitation via contralateral median nerve stimulation (Supplementary Fig. 10). Additionally, comparing baseline (FUS−FES−) to tFUS (FUS+FES−) reveals no unintended effects or evoked potentials due to ultrasound stimulation. Together, these results confirm effective EEG electrode placement around the pre- and post-central gyrus of S1, with strong SEP signals, and successful targeting and suppression of SEP using MiniUlTra. Further works in the future using high density EEG recordings with source localization in conjunction with MiniUlTra would provide insight on its' potential towards changes in cognitive and mood disorders[107–110], pain management[111–113], or rehabilitative motor functions[114,115].

In conclusion, wearable ultrasound stimulation devices hold significant promise for the long-term treatment of chronic diseases like Parkinson's disease, essential tremor, epilepsy, and depression (Supplementary Fig. 12). These devices offer non-invasive, spatiotemporal targeted modulation of neural activity, potentially improving disease symptoms without the drawbacks of medications or surgery. Their non-invasive nature and wearability also suggest the potential for home-based therapy, although continued research is essential to optimize treatment protocols and ensure long-term safety and efficacy across diverse patient populations. As such, future study would be beneficial in evaluating the long-term applications of MiniUlTra in neuromodulation.

Methods

Ethics statement

This study involving human participants was conducted in accordance with the ethical principles outlined in the Declaration of Helsinki. Approval for the research was obtained from the Institutional Review Board (IRB) at The University of Texas at Austin (UT Austin) under the study (STUDY00003279), ensuring compliance with ethical guidelines and regulations. Informed consent was obtained from all participants prior to their involvement in the study. Confidentiality and data protection measures were strictly followed to safeguard participant privacy.

Fabrication of SFAT-ACFAL

Geometric shape and radius of the ACFAL was determined first by selection of 10 mm focal depth according to the equations governed by Fresnel lens[116], which was then implemented into finite element analysis software for simulation (COMSOL Multiphysics 6.0, COMSOL Inc.) to determine acoustic field distribution (Supplementary Fig. 13 and Tables 6 and 7). Optimization of PDMS and air-cavity thickness was performed with reference to feasibility of microfabrication (Supplementary Fig. 13).

Mold glass substrates were initially patterned by first laminating 36 μm thick copper tape (1125, 3 M) onto adhesive interlayer (Ultra 582U, TransferRite), which was then laminated onto an adhesive backing layer (GXF341, DigiClear Plus). The laminated copper tape was then negatively patterned using laser etching (LPKF, U4 Laser) and transferred printed onto the glass substrate (Supplementary Fig. 14i).

Patterned mold glass substrates were cleaned and prepared by first submerging into a beaker filled with acetone and sonicated to remove particulates for 5 min. Substrates were then removed, rinsed with distilled water and submerged in methanol for 5 min of sonication. The substrates were then rinsed with distilled water before blow dried with purified nitrogen gas. Substrate was spin-coated with a sacrificial layer (Omnicoat, Kayaku Advanced Materials) for 30 s at 1000 RPM and 3 min of planarization before soft-baking at 200 °C on a hotplate. The parameters were determined empirically through patterning and measurement of thickness using profilometer (Supplementary Fig. 15) Subsequently, substrates were then spin-coated with 5 ml of PDMS (Sylgard 184); prepared by mixing 1:10 of curing agent with base elastomer and desiccated for 1 h at 500 RPM to achieve ~200 μm thickness and cured on a hotplate at 90 °C for 35 min. Substrates were then placed in acetone filled beakers and sonicated for 5 min each to release the patterned PDMS mold (Supplementary Fig. 14ii). Using tweezers, the patterned PDMS layer was carefully removed and placed onto a temporary glass substrate, which was then trimmed with medical scalpel. PZT (DL-47, Del Piezo) was cleaned by first submerging into a beaker filled with acetone and sonicated to remove particulates for 5 min. Substrates were then removed, rinsed with distilled water and submerged in methanol for 5 min of sonication. The substrates were then rinsed with distilled water before blow dried with purified nitrogen gas. Two milliliters of prepared PDMS was spin-coated onto the surface of PZT at 2000 RPM for 30 s to achieve a thickness of 40 μm; cured at 90 °C for 30 min (Supplementary Fig. 14iii).

Next, the released patterned PDMS layer and coated-PDMS PZT was treated with Reactive Ion Etching (RIE) O_2 plasma treatment for 25 s (30 W @ 30% O_2, 30 SCCM) to remove organic hydrocarbons on the surface and create silanol (SiOH) functional groups, effectively increasing the wettability and rendering surface more hydrophilic[117]. The patterned PDMS layer was then reversely bonded onto the coated-PDMS PZT by attachment and applying 1 kg weight simultaneously on a 120 °C hotplate for 5 min (Supplementary Fig. 14iv).

Acoustic field mapping of SFAT-ACFAL

Mapping. The SFAT-ACFAL device was mounted on a submersible stand in a degassed distilled glass water tank. Acoustic intensity and waveform were measured using a calibrated capsule hydrophone (HGL-0200, Onda) mounted on a three-axis stage system, which was connected to an oscilloscope (SDS 1204-XE, Siglent) via a signal preamplifier (AG-2010, Onda) interfaced to a custom MATLAB program

for automated 3D scanning and signal processing (Supplementary Fig. 16). The device was controlled and actuated by a commercially available ultrasound system (BBBoq, Image Guided Therapy Systems). Acoustic field scans without human skulls were first performed at 500 μm increments (0–40 mm from transducer in a 40 mm × 40 mm grid workspace). Focal depth and spatial peak locations were obtained from the acquired acoustic field scans axially and radially. Subsequently, the human skull (Skull Unlimited International Inc., 8-mm thick human cortical bone, rehydrated for 24 h in phosphate buffer solution) obtained was inserted in between the transducer and hydrophone using the same scan procedures. Due to the curvature and inhomogeneous geometry, acoustic field scans were performed at 500 μm increments (~10–40 mm from the transducer in a 40 mm × 40 mm grid workspace) to avoid collision between transducer, skull, and hydrophone.

tFUS waveform. Generation of tFUS profile from SFAT-ACFAL was performed using a 40-W high-voltage biphasic ultrasound function generator system (BBBoq, Image Guided Therapy System) controlled and pulsed by an external Arduino trigger. Briefly, the function generator was set to deliver individual pulses at 360 μs ON and 640 μs OFF with center frequency of 650 kHz (Fig. 2e). The Arduino was then programmed to trigger the function generator at a PRF of 1 kHz and pulse duration of 500 ms ON and 500 ms OFF.

Electrical characteristics. SFAT-ACFAL was connected to an impedance spectrum analyzer (SP300, BioLogic) using a two-electrode connection configuration. Impedance of the device was measured from 0 to 1 MHz to validate resonant frequencies. Fundamental harmonics and phases were identified in addition to the desired 650 kHz (Fig. 2h).

Thermal heating. SFAT-ACFAL was placed facing upwards on a 3D-printed mounted stand, where the superficial side of the human skull was placed in contact with the transducer using ultrasound coupling gel (Aquasonic 100, Parker). Three stimulation paradigms with varying duty cycle and pulse duration were used (100 μs ON/900 μs OFF, 360 μs ON/640 μs OFF, 500 μs ON/500 μs OFF) for 10 min to compare and observe the thermal heating effects from tFUS (Fig. 2g). An infrared camera (One Edge, FLIR) was used to record three points in a triangular configuration surrounding the targeting area on the inferior side of the human skull (Supplementary Figs. 2 and 3).

Synthesis and integration of bioadhesive hydrogel to SFAT

Materials and fabrication of bioadhesive hydrogel. The preparation of the bioadhesive hydrogel started with mixing the hydrogel solution. First, AMPS (Sigma-Aldrich) was dissolved in deionized (DI) water at a 1:1 ratio using a vortex mixer for 30 s. Subsequently, glycerol (Alfa Aesar) with 20 wt% was added to the AMPS/DI water mixture using a vortex mixer for 30 s. N, N′-Methylenebis(acrylamide) (MBAA crosslinker, Sigma-Aldrich) with ~0.16 wt% was then added and mixed for 60 s. Irgacure 2959 (2-Hydroxy-4′-(2-hydroxyethoxy)-2-methylpropiophenone 98%, Sigma-Aldrich) with ~0.59 wt%, serving as the photoinitiator, was mixed for 30 s. The solution was stirred additionally for 30 min. To improve adhesion force between PDMS and hydrogel, the PDMS-based ACFAL integrated with SFAT was treated with benzophenone (BZP) by first mixing 10% w/w BZP with acetone for 60 s via vortexing followed by 60 s of sonication to ensure complete incorporation of BZP in solvent. Subsequently, the solution was pipetted onto the surface of PDMS and exposed to air for solution to evaporate for 10 min. Upon complete evaporation, the PDMS surface was washed gently with DI water three times to remove excess BZP crystalline solids formed and dried with O_2 air gun before depositing the bioadhesive hydrogel for curing. Lastly, bioadhesive hydrogel was integrated with SFAT-ACFAL by cross-linking the hydrogel solution under UV light for 15 min (~ 4.21 J).

Characterization of bioadhesive hydrogel

Adhesion strength of bioadhesive hydrogel with skin and PDMS. The adhesion strength of the bioadhesive hydrogel was evaluated modified ASTM F2255-05 and ASTM F2256-05 methods through custom-developed and integrated testing machine (FB5, Torbal) with 90°-peeling off test. The samples were prepared with dimensions of 20 × 50 × 2 mm (width × length × thickness), and the backside of each sample was affixed with Kapton film (7413D, 3 M) to prevent stretching during peeling. To measure the adhesion between the skin and bioadhesive hydrogel, the samples were gently attached onto a skin, and then peeled off at a 90° angle from the skin at a speed of 68 mm/min. To measure the adhesion between PDMS and bioadhesive hydrogel, PDMS was initially deposited and cured on a glass substrate mold (width: 50 mm, length: 76 mm). Then, a BZP treatment process was conducted. Using a similar 90°-peeling off test, the substrate was mounted and performed to compare adhesion force with and without BZP-treatment between the hydrogel and PDMS (Fig. 3i).

Weight loss. To measure the dehydration characteristics of the hydrogel, a weight loss test was conducted. A circular-shaped bioadhesive hydrogel and a commercial gel (Aquasonic 100, Parker) sample were prepared (diameter: 19 mm, thickness: 1 mm). The weight of each was measured over time both in a typical room environment (~41%, ~23 °C) and inside a container with high humidity (~65%, ~23 °C) (Supplementary Figs. 5–7). The weight loss of the samples (W_l) was calculated using the equation $W_l\ (\%) = (W_t - W_i)/W_i \times 100$, where W_i and W_t denote, respectively, the initial weight of the sample and the weight of the sample at different times.

Acoustic attenuation of hydrogel. To prevent the bioadhesive hydrogel and commercial gel from swelling and dissipating in the water during ultrasound measurement, a thin Ecoflex cap was fabricated with a mold to wrap around hydrogel/gel (Supplementary Fig. 17). The internal thickness of the Ecoflex cap was adjustable to control the thickness of bioadhesive hydrogel or commercial gel (0.5–2.5 mm thick). The Ecoflex cap was then filled with the hydrogel or commercial gel and attached to a pristine PZT (DL-47, Del Piezo) and mounted on a submersible stand in a degassed distilled water tank. Acoustic intensity and waveforms were measured using a calibrated capsule hydrophone (HGL-0200, Onda) mounted a three-axis stage system at a fixed distance of 10 mm from the PZT uniaxially in the water tank.

Acoustic impedance and speed of hydrogel. Acoustic properties of the bioadhesive hydrogel were characterized by measuring and estimating the acoustic time-of-flight difference of ultrasound transmission through water, PET, and hydrogel between transducer and hydrophone. A single cycle sine wave pulse was generated using a 3-level beamformer transmitter circuit (TX7316, Texas Instrument) with a supplied driving voltage of ± 20 V. To measure the acoustic time-of-flight of the hydrogel, a 3-mm thick hydrogel was prepared with a mold consisting of PET film and Ecoflex frame (Supplementary Figs. 18 and 19) and measurements were performed over a period of 7 days. The purpose of the Ecoflex frame was to maintain the thickness of the hydrogel and to prevent the penetration of the water into the hydrogel when measuring in the water tank. Between measurements, the Ecoflex frame was removed temporarily, and the hydrogel samples were stored in a room environment (humidity: ~30%, temperature: ~23 °C). Then, when measurements were taken again, the Ecoflex frame was placed around the hydrogel again to prevent water from entering the hydrogel. The acoustic time-of-flight was measured by placing the hydrogel samples between transducer and hydrophone in a water

tank. The acoustic speed of the hydrogel was estimated by following equations[52]:

$$c_{hydrogel} = \frac{T_{hydrogel}}{\left(\frac{T_{hydrogel} + 2T_{PET}}{c_{water}}\right) - \frac{2T_{PET}}{c_{PET}} - \Delta t_{PET} + \Delta t_{PET+Hydrogel}} \quad (1)$$

Where $T_{Hydrogel}$ is the thickness of the bioadhesive hydrogel, T_{PET} is the thickness of the PET film, c_{Water} is the speed of sound in water (1500 m/s), c_{PET} is the speed of sound in PET film (polyethylene, high density: 2430 m/s[118]), ΔT_{PET} is ToF difference between with and without PET film, $\Delta T_{PET+Hydrogel}$ is ToF difference between with and without hydrogel samples.

$$Z_{Hydrogel} = \rho_{Hydrogel} \times c_{Hydrogel} \quad (2)$$

Where $Z_{Hydrogel}$ is the acoustic impedance of the bioadhesive hydrogel, $\rho_{Hydrogel}$ is the density of the hydrogel, $c_{Hydrogel}$ is the speed of sound of the hydrogel.

Long-term acoustic stability. To assess the long-term acoustic stability of the bioadhesive hydrogel, the ultrasound intensity of the bioadhesive hydrogel integrated SFAT was measured over time. The number of circular-shaped hydrogels were prepared and stored in a container with high humidity (~65%, ~23 °C). At specific time intervals, each bioadhesive hydrogels were taken out of the container and attached to a bare PZT transducer. All measurements were conducted under the deionized water. To prevent rapid swelling of the AMPS-based bioadhesive hydrogel upon contact with water, bioadhesive on the bare PZT transducer was covered with a thin Ecoflex cap (thickness: 0.5 mm). Then, the attenuation of ultrasound intensity due to the bioadhesive hydrogel over time was measured using a custom setup 3-axis hydrophone acoustic scanning system.

Device integration of MiniUlTra

Fabricated SFAT-ACFAL was connected via low temperature solder (NP510-LT HRL1, Kester) to a BNC cable and housed in a custom-designed 3D printed casing (PLA Galaxy, Prusa), which was lined with copper shielding (1181, 3 M) and grounded to the BNC shielding layer for electromagnetic shielding purposes. To integrate SFAT-ACFAL with the bioadhesive hydrogel, the hydrogel solution was then poured to a thickness of 1 mm. Subsequently, the bioadhesive hydrogel on the SFAT-ACFAL was cross-linked under UV light for 15 min. Finally, the integrated device was completed by removing the mold (Supplementary Fig. 14v).

Long-term stability of MiniUlTra. Fabricated MiniUlTra was covered with Ecoflex cap (Supplementary Fig. 17) and cured to seal and protect the bioadhesive hydrogel grafted on the transducer from swelling. The device was then submerged into a degassed distilled water tank (Supplementary Fig. 17) and free-field (without human skull) measurement were performed across 28 days (Days 1, 3, 5, 7, 14, and 28) to demonstrate beam-focusing and focal depth stability of MiniUlTra (Supplementary Fig. 20).

Characterization of tFUS on sensory-evoked potentials in S1 using SFAT-ACFAL

Participants. All procedures were designed in accordance with the Declaration of Helsinki and relevant ethical regulations regarding human research. The IRB at University of Texas at Austin approved all experimental procedures under the study (STUDY00003279). Eight healthy volunteers (7 male, 1 female, aged 24–38 with a mean age of 29.1 ± 4.1 years) provided written informed consent to participate in the study and were recruited from around the university area in Austin, Texas. Volunteers were screened for contraindications and neurological impairment and all subjects were right-hand dominant (Supplementary Table 8).

Experimental setup. Participants were positioned and seated in an adjustable height chair, where their right forearm is fully extended and supported in supination. Four 10–20 EEG electrode sites (C3, CP1, P3, CP5) were connected for recording somatosensory evoked potentials. During testing, subjects were initially stimulated by FES with varying currents (8–25 mA, 200 μs) to obtain the minimum threshold necessary to elicit muscle contraction of the right contralateral side. The SFAT-ACFAL was applied topically to CP3 manually with administration of ultrasound gel (Aquasonic 100, Parker) as interface to the scalp, which was then held in place using medical tape. Additionally, three electrical stimulation electrodes (2" Round, Reserv) were placed on the right contralateral arm (ground electrode on elbow, bipolar electrodes axially paired on the wrist via palpation of median nerve). The electrodes were connected to a functional electrical stimulation (FES) system (RehaMove3, Hasomed) for median nerve stimulation (MN), which was controlled externally by custom Python software.

tFUS treatment condition stimulation occurring 100 ms before MN stimuli (360 μs ON and 640 μs OFF, PRF 1 kHz, Pulse Duration 500 ms ON 500 ms OFF) was controlled by programming of microcontroller (Uno, Arduino), which was connected to trigger the ultrasound generator (BBBoq, Image Guided Therapy System), FES system (MN stimuli), and EEG amplifier for time-locked epoch events during somatosensory evoked potentials (SEP) (Supplementary Fig. 21). Custom Python code was developed to integrate all systems together in addition to use of LabStreamingLayer to stream and log EEG data into dataframe with external data including trigger and metadata. Subjects were then subjected to three blocks of trials, where each block consisted of four trials (FUS−/FES−, FUS−/FES+, FUS+/FES−, FUS+/FES+) and each trial lasted 3 min. Within each trial, 30 s of baseline recording occurs before 120 s of sham/FUS followed by 30 s of rest recording to ensure sufficient buffered data for post-recording cleaning. Total recording session time was approximately 1 h.

EEG placement and artifact mitigation. Subjects recruited were invited to a dedicated EEG recording room with minimal electronics for minimizing electromagnetic interferences. Tape ruler was used to measure the distance between nasion-to-inion and left-right pre-auricular points to determine electrode positioning according to the 10–20 system for EEG recording. Marker was used to indicate the position of C3, CP1, P3, CP5 for EEG and CP3 for tFUS targeting (Fig. 4b). Subsequently, rubbing alcohol was applied carefully at the sites before conductive hydrogel electrodes (H124SG, Kendall) were applied carefully to the scalp to ensure minimal obstruction of hair. Impedance per electrode was measured using commercial amplifier (eego MyLab, AntNeuro) to ensure it is less than 10 kΩ. EEG data were digitized at 512 Hz and stored for offline analysis. To ensure artifacts from electromagnetic interference generated by piezoelectric in MiniUlTra, common grounding connecting the microcontroller, EEG amplifier, and ultrasound generator was performed. Furthermore, the copper shielding on MiniUlTra was also connected to the same ground to ensure complete grounding of the device and mitigating leakage current path through the body (Supplementary Fig. 22).

Statistical analysis of somatosensory evoked potentials. Digitized EEG data were analyzed offline by first filtering using a third-order Butterworth bandpass filter (2–90 Hz) followed by a first-order Butterworth bandstop filter (59–61 Hz) to remove DC offsets, mains interference, and high frequency noises[119–122]. A total of 120 epochs per trial recorded was then extracted using custom MATLAB code using triggered signals as markers. Briefly, data were epoched around median nerve stimulus trigger, 200 ms prior up to 500 ms

after the trigger was extracted as a single epoch for analysis. Subsequently, the data was baseline corrected by subtracting the mean values from = −200 ms to 0 ms. For each epoch, inspection of artifacts using rejection criteria of absolute peak-to-peak amplitude threshold greater than 75 μV will be removed. Grand averaged epochs across 8 subjects were obtained to determine the effects of sham and FUS in SEP using SFAT-ACFAL elicited by MN stimuli. EEG biomarkers N20, P27, N33, P50, N70, P100, and N140 were extracted by obtaining the mean amplitude ± 2 ms the desired biomarker time event due to the difficulty to reliably identify SEP peaks accurately per trial. Statistical analyses were performed on mean peak-to-peak amplitudes for the N20/P27, N33/P27, P50/N33, N70/P50, P100/N70, N140/P100 and long potential (LP) components (Supplementary Tables 1–4). These data were averaged across all trials and subjects and presented as mean ± s.e.m for different group conditions. Non-parametric statistical test using Wilcoxon signed-rank test was applied for SEP complexes to determine significance of treatment conditions.

Time-frequency analysis of short-latency somatosensory evoked potentials. Time frequency analysis was performed (MATLAB R2021a, The MathWorks) to decompose effects and changes in frequency spectrum due to S1 targeting using tFUS with SFAT-ACFAL as a function of time[123]. Short-time Fourier transform was used with a window size of 4.8 ms and 2.3 ms overlap through Hamming window approach. Power of spectral data was then converted into power (dB). Comparison between treatment groups was performed by comparing spectral epochs to observe dynamic changes in power with respect to frequency bands (Supplementary Fig. 9).

Long-term demonstration of tFUS neuromodulation of MiniUlTra

Participants. All procedures were designed in accordance with the Declaration of Helsinki and relevant ethical regulations regarding human research. The IRB at University of Texas at Austin approved all experimental procedures under the study (STUDY00003279). Eight healthy volunteers (8 male, aged 26–37 with a mean age of 30.5.2 ± 3.9 years) provided written informed consent to participate in the study and were recruited from around the university area in Austin, Texas. Volunteers were screened for contraindications and neurological impairment and all subjects were right-hand dominant (Supplementary Table 9).

Experimental setup. Subjects were invited to S1 targeted tFUS stimulation using MiniUlTra (SFAT-ACFAL integrated with bioadhesive hydrogel) for long-term study (Day 1, 7, and 28). For each session, subjects were pre-screened for contraindications before beginning the experiment. Four 10–20 EEG electrode sites (C3, CP1, P3, CP5) were connected for recording somatosensory evoked potentials (Fig. 4b) by marking positioning using 10–20 EEG headcap. Minimum threshold for right contralateral hand movement due to MN stimulation was performed to obtain the minimum threshold necessary to elicit muscle contraction of the right contralateral side. The MiniUlTra was applied to CP3 and held in place independently by its adhesive nature (Supplementary Fig. 23). For EEG recording stability, additional medical tape was used to fix EEG electrodes and transducers to prevent motion artifacts. Three electrical stimulation electrodes (2" Round, Reserv) were placed on the right contralateral arm (one on wrist, one 1" distal from wrist electrode, and one on elbow) for S1 targeting (Fig. 4a). The electrodes were connected to a functional electrical stimulation (FES) system (RehaMove3, Hasomed) for MN stimulation.

tFUS treatment and sham conditions performed identically where subjects were subjected to five blocks of trial, where each block consisted of four trials (FUS−/FES+; Sham, FUS+/FES+; Treatment, FUS −FES−; Negative Control, FUS+FES−; Positive Control) and each trial lasted 3 min. Total recording session time was approximately 1 h.

Long-term effects and post ad-hoc analysis. Questionnaires were provided to subjects to examine the comfortability, pain, sensitivity, and sensation of FUS neuromodulation using MiniUlTra (Supplementary Fig. 11A). Furthermore, subjects were asked per session to identify which trials they believe were the FUS+ trials to determine if sensations reported were due to placebo (Supplementary Fig. 11C, D).

Statistical analysis of MiniUlTra's long-term efficacy in somatosensory evoked potential suppression. A total of 120 epochs per trial recorded was then extracted using custom MATLAB code using triggered signals as markers. Grand averaged epochs across 8 subjects and 20 trials were obtained to determine the effects of sham and FUS in SEP using MiniUlTra elicited by MN stimuli. EEG biomarkers N20 and P27 were extracted by obtaining the mean amplitude ± 2 ms the desired biomarker time event due to the difficulty to reliably identify SEP peaks accurately per trial. Statistical analyses were performed on mean peak-to-peak amplitudes for the N20/P27 (Supplementary Table 5). These data were averaged across all trials and subjects and presented as mean ± s.e.m for different group conditions. Šídák multiple comparison One-way ANOVA was applied for SEP complexes to determine effects of sham (FUS−FES+) and stimulation (FUS+FES+) groups across multiple sessions compared to the use of commercial gel over long-term[124].

Reporting summary

Further information on research design is available in the Nature Portfolio Reporting Summary linked to this article.

Data availability

Additional data supporting the study's findings are included in the article and its supplementary information and supplementary data. Source data are provided and included. Source data are provided with this paper.

Code availability

The codes used for this study are available on GitHub at https://github.com/kevintang725/MiniUlTra-LSL (https://doi.org/10.5281/zenodo.15258560).

References

1. Marras, C. et al. Prevalence of Parkinson's disease across North America. *npj Parkinson's Dis.* **4**, 1–7 (2018).
2. Matthews, K. A. et al. Racial and ethnic estimates of Alzheimer's disease and related dementias in the United States (2015–2060) in adults aged ≥65 years. *Alzheimers Dement.* **15**, 17–24 (2019).
3. Visser-Vandewalle, V. et al. Deep brain stimulation for obsessive–compulsive disorder: a crisis of access. *Nat. Med.* **28**, 1529–1532 (2022).
4. Mar-Barrutia, L. et al. Deep brain stimulation for obsessive-compulsive disorder: a systematic review of worldwide experience after 20 years. *World J. Psychiatry* **11**, 659–680 (2021).
5. Volkmann, J. Deep brain stimulation for the treatment of Parkinson's disease. *J. Clin. Neurophysiol.* **21**, 6–17 (2004).
6. Benabid, A. L. Deep brain stimulation for Parkinson's disease. *Curr. Opin. Neurobiol.* **13**, 696–706 (2003).
7. Deuschl, G. et al. A randomized trial of deep-brain stimulation for Parkinson's disease. *N. Engl. J. Med.* **355**, 896–908 (2006).
8. Flora, E. D., Perera, C. L., Cameron, A. L. & Maddern, G. J. Deep brain stimulation for essential tremor: a systematic review. *Mov. Disord.* **25**, 1550–1559 (2010).
9. Blomstedt, P., Hariz, G.-M., Hariz, M. I. & Koskinen, L.-O. D. Thalamic deep brain stimulation in the treatment of essential tremor: a

long-term follow-up. *Br. J. Neurosurg*. https://doi.org/10.1080/02688690701552278 (2007).
10. Baizabal-Carvallo, J. F., Kagnoff, M. N., Jimenez-Shahed, J., Fekete, R. & Jankovic, J. The safety and efficacy of thalamic deep brain stimulation in essential tremor: 10 years and beyond. *J. Neurol. Neurosurg. Psychiatry* **85**, 567–572 (2014).
11. Hubble, J. P. et al. Deep brain stimulation for essential tremor. *Neurology* **46**, 1150–1153 (1996).
12. Koller, W. C., Lyons, K. E., Wilkinson, S. B., Troster, A. I. & Pahwa, R. Long-term safety and efficacy of unilateral deep brain stimulation of the thalamus in essential tremor. *Mov. Disord.* **16**, 464–468 (2001).
13. Li, M. C. H. & Cook, M. J. Deep brain stimulation for drug-resistant epilepsy. *Epilepsia* **59**, 273–290 (2018).
14. Loddenkemper, T. et al. Deep brain stimulation in epilepsy. *J. Clin. Neurophysiol.* **18**, 514–532 (2001).
15. Boon, P. et al. Deep brain stimulation in patients with refractory temporal lobe epilepsy. *Epilepsia* **48**, 1551–1560 (2007).
16. Theodore, W. H. & Fisher, R. S. Brain stimulation for epilepsy. *Lancet Neurol.* **3**, 111–118 (2004).
17. Cury, R. G. et al. Thalamic deep brain stimulation for tremor in Parkinson disease, essential tremor, and dystonia. *Neurology* **89**, 1416–1423 (2017).
18. Vercueil, L. et al. Deep brain stimulation in the treatment of severe dystonia. *J. Neurol.* **248**, 695–700 (2001).
19. Vidailhet, M. et al. Bilateral deep-brain stimulation of the globus pallidus in primary generalized dystonia. *N. Engl. J. Med.* **352**, 459–467 (2005).
20. Denys, D. et al. Deep brain stimulation of the nucleus accumbens for treatment-refractory obsessive-compulsive disorder. *Arch. Gen. Psychiatry* **67**, 1061–1068 (2010).
21. Hariz, M. I. Complications of deep brain stimulation surgery. *Mov. Disord.* **17**, S162–S166 (2002).
22. Salatino, J. W., Ludwig, K. A., Kozai, T. D. Y. & Purcell, E. K. Glial responses to implanted electrodes in the brain. *Nat. Biomed. Eng.* **1**, 862–877 (2017).
23. Cohen, S. L., Bikson, M., Badran, B. W. & George, M. S. A visual and narrative timeline of US FDA milestones for Transcranial Magnetic Stimulation (TMS) devices. *Brain Stimul.* **15**, 73–75 (2022).
24. Elahi, B., Elahi, B. & Chen, R. Effect of transcranial magnetic stimulation on Parkinson motor function—Systematic review of controlled clinical trials. *Mov. Disord.* **24**, 357–363 (2009).
25. Freitas, C., Mondragón-Llorca, H. & Pascual-Leone, A. Noninvasive brain stimulation in Alzheimer's disease: systematic review and perspectives for the future. *Exp. Gerontol.* **46**, 611–627 (2011).
26. McNamara, B., Ray, J. L., Arthurs, O. J. & Boniface, S. Transcranial magnetic stimulation for depression and other psychiatric disorders. *Psychol. Med.* **31**, 1141–1146 (2001).
27. Richter, L. *Robotized Transcranial Magnetic Stimulation* (Springer Science & Business Media, 2014).
28. Toschi, N., Welt, T., Guerrisi, M. & Keck, M. E. A reconstruction of the conductive phenomena elicited by transcranial magnetic stimulation in heterogeneous brain tissue. *Phys. Med.* **24**, 80–86 (2008).
29. Ravazzani, P., Ruohonen, J., Grandori, F. & Tognola, G. Magnetic stimulation of the nervous system: induced electric field in unbounded, semi-infinite, spherical, and cylindrical media. *Ann. Biomed. Eng.* **24**, 606–616 (1996).
30. Thielscher, A. & Kammer, T. Linking physics with physiology in TMS: a sphere field model to determine the cortical stimulation site in TMS. *Neuroimage* **17**, 1117–1130 (2002).
31. Fregni, F., Simon, D. K., Wu, A. & Pascual-Leone, A. Non-invasive brain stimulation for Parkinson's disease: a systematic review and meta-analysis of the literature. *J. Neurol. Neurosurg. Psychiatry* **76**, 1614–1623 (2005).
32. Hamid, P., Malik, B. H. & Hussain, M. L. Noninvasive transcranial magnetic stimulation (TMS) in chronic refractory pain: a systematic review. *Cureus* **11**, e6019 (2019).
33. Laxton, A. W. & Lozano, A. M. Deep Brain Stimulation for the treatment of Alzheimer disease and dementias. *World Neurosurg.* **80**, S28.e1–S28.e8 (2013).
34. Bowary, P. & Greenberg, B. D. Noninvasive Focused Ultrasound for Neuromodulation: A Review. *Psychiatr. Clin. North Am.* **41**, 505–514 (2018).
35. Lipsman, N. et al. MR-guided focused ultrasound thalamotomy for essential tremor: a proof-of-concept study. *Lancet Neurol.* **12**, 462–468 (2013).
36. Martin, E., Jeanmonod, D., Morel, A., Zadicario, E. & Werner, B. High-intensity focused ultrasound for noninvasive functional neurosurgery. *Ann. Neurol.* **66**, 858–861 (2009).
37. Meng, Y. et al. Resting state functional connectivity changes after MR-guided focused ultrasound mediated blood-brain barrier opening in patients with Alzheimer's disease. *Neuroimage* **200**, 275–280 (2019).
38. Nicodemus, N. E. et al. Focused transcranial ultrasound for treatment of neurodegenerative dementia. *Alzheimer's Dement.: Transl. Res. Clin. Interventions* **5**, 374–381 (2019).
39. Jeong, H. et al. A pilot clinical study of low-intensity transcranial focused ultrasound in Alzheimer's disease. *Ultrasonography* **40**, 512–519 (2021).
40. Beisteiner, R. et al. Transcranial pulse stimulation with ultrasound in Alzheimer's disease—A new navigated focal brain therapy. *Adv. Sci. Lett.* **7**, 1902583 (2020).
41. Dörl, G., Matt, E. & Beisteiner, R. Functional specificity of TPS brain stimulation effects in patients with Alzheimer's disease: a follow-up fMRI analysis. *Neurol. Ther.* **11**, 1391–1398 (2022).
42. Bubrick, E. J. et al. Transcranial ultrasound neuromodulation for epilepsy: a pilot safety trial. *Brain Stimul.* **17**, 7–9 (2024).
43. Lee, C.-C. et al. Pilot study of focused ultrasound for drug-resistant epilepsy. *Epilepsia* **63**, 162–175 (2022).
44. Stern, J. M. et al. Safety of focused ultrasound neuromodulation in humans with temporal lobe epilepsy. *Brain Stimul.* **14**, 1022–1031 (2021).
45. Pellow, C., Pichardo, S. & Pike, G. B. A systematic review of preclinical and clinical transcranial ultrasound neuromodulation and opportunities for functional connectomics. *Brain Stimul.* **17**, 734–751 (2024).
46. La, T.-G. & Le, L. H. Flexible and wearable ultrasound device for medical applications: a review on materials, structural designs, and current challenges. *Adv. Mater. Technol.* **7**, 2100798 (2022).
47. Pang, C., Lee, C. & Suh, K.-Y. Recent advances in flexible sensors for wearable and implantable devices. *J. Appl. Polym. Sci.* **130**, 1429–1441 (2013).
48. Rathod, V. T. A Review of acoustic impedance matching techniques for piezoelectric sensors and transducers. *Sensors* **20**, 4051 (2020).
49. Afzal, S. et al. Preparation and evaluation of polymer-based ultrasound gel and its application in ultrasonography. *Gels* **8**, 42 (2022).
50. Hu, Y.-Y. et al. Transcranial low-intensity ultrasound stimulation for treating central nervous system disorders: a promising therapeutic application. *Front. Neurol.* **14**, 1117188 (2023).
51. Wang, C. et al. Bioadhesive ultrasound for long-term continuous imaging of diverse organs. *Science* **377**, 517–523 (2022).
52. Lee, S.-M. et al. Calcium-modified silk patch as a next-generation ultrasound coupling medium. *ACS Appl. Mater. Interfaces* **13**, 55827–55839 (2021).
53. Molerón, M., Serra-Garcia, M. & Daraio, C. Acoustic Fresnel lenses with extraordinary transmission. *Appl. Phys. Lett.* **105**, 114109 (2014).

54. White, P. J., Clement, G. T. & Hynynen, K. Local frequency dependence in transcranial ultrasound transmission. *Phys. Med. Biol.* **51**, 2293–2305 (2006).
55. Hayner, M. & Hynynen, K. Numerical analysis of ultrasonic transmission and absorption of oblique plane waves through the human skull. *J. Acoust. Soc. Am.* **110**, 3319–3330 (2001).
56. Legon, W. et al. Transcranial focused ultrasound modulates the activity of primary somatosensory cortex in humans. *Nat. Neurosci.* **17**, 322–329 (2014).
57. Kim, H.-C., Lee, W., Weisholtz, D. S. & Yoo, S.-S. Transcranial focused ultrasound stimulation of cortical and thalamic somatosensory areas in human. *PLoS ONE* **18**, e0288654 (2023).
58. Deffieux, T. & Konofagou, E. E. Numerical study of a simple transcranial focused ultrasound system applied to blood-brain barrier opening. *IEEE Trans. Ultrason. Ferroelectr. Freq. Control* **57**, 2637–2653 (2010).
59. Murty, O. Variability in thickness of skull bones and sternum. *J. Forensic Med. Toxicol.* **26**, 26–31 (2009).
60. Gâteau, J. et al. Transcranial ultrasonic therapy based on time reversal of acoustically induced cavitation bubble signature. *IEEE Trans. Biomed. Eng.* **57**, 134–144 (2010).
61. Lee, W., Weisholtz, D. S., Strangman, G. E. & Yoo, S.-S. Safety review and perspectives of transcranial focused ultrasound brain stimulation. *Brain Neurorehabil.* **14**, e4 (2021).
62. Rahnama, R. Analyzing the piezoelectric rings resonance modes for bandwidth ultrasonic transducers. *Microsyst. Technol.* **26**, 1925–1929 (2020).
63. Ye, H. & De, S. Thermal injury of skin and subcutaneous tissues: A review of experimental approaches and numerical models. *Burns* **43**, 909–932 (2017).
64. Luo, H. et al. Forward osmosis with electro-responsive P(AMPS-co-AM) hydrogels as draw agents for desalination. *J. Memb. Sci.* **593**, 117406 (2020).
65. Hsieh, J.-C. et al. Design of an injectable, self-adhesive, and highly stable hydrogel electrode for sleep recording. *Device* **2**, 100182 (2023).
66. Hsieh, J.-C. et al. A highly stable electrode with low electrode-skin impedance for wearable brain-computer interface. *Biosens. Bioelectron.* **218**, 114756 (2022).
67. Lee, C.-J. et al. Ionic conductivity of polyelectrolyte hydrogels. *ACS Appl. Mater. Interfaces* **10**, 5845–5852 (2018).
68. Ashkani, M., Bouhendi, H., Kabiri, K. & Rostami, M. R. Synthesis of poly (2-acrylamido-2-methyl propane sulfonic acid) with high water absorbency and absorption under load (AUL) as concrete grade superabsorbent and its performance. *Constr. Build. Mater.* **206**, 540–551 (2019).
69. Sekizkardes, B., Su, E. & Okay, O. Mechanically strong superabsorbent terpolymer hydrogels based on AMPS via hydrogen-bonding interactions. *ACS Appl. Polym. Mater.* https://doi.org/10.1021/acsapm.2c02085 (2023).
70. Chen, H. J. et al. Moisture retention of glycerin solutions with various concentrations: a comparative study. *Sci. Rep.* **12**, 10232 (2022).
71. Shen, G. et al. A novel flexible hydrogel electrode with a strong moisturizing ability for long-term EEG recording. *J. Neural Eng.* **18**, 066047 (2021).
72. Zhang, K. et al. Metagel with broadband tunable acoustic properties over air–water–solid ranges. *Adv. Funct. Mater.* **29**, 1903699 (2019).
73. Laugier, P. & Haïat, G. Introduction to the physics of ultrasound. *Bone Quantitative Ultrasound* 29–45 (2011).
74. Lee, S.-M. Calcium-modified silk patch as a next-generation ultrasound coupling medium. *ACS Appl. Mater. Interfaces* **13**, 55827–55839 (2021).
75. Prokop, A. F. Polyacrylamide gel as an acoustic coupling medium for focused ultrasound therapy. *Ultrasound Med. Biol.* **29**, 1351–1358 (2003).
76. Bloomfield, P. E., Lo, W. J. & Lewin, P. A. Experimental study of the acoustical properties of polymers utilized to construct PVDF ultrasonic transducers and the acousto-electric properties of PVDF and P(VDF/TrFE) films. *IEEE Trans. Ultrason. Ferroelectr. Freq. Control* **47**, 1397–1405 (2000).
77. Carlson, J., van Deventer, J., Scolan, A. & Carlander, C. Frequency and temperature dependence of acoustic properties of polymers used in pulse-echo systems. *Proc. IEEE Ultrason. Symp.***1**, 885–888 (2003).
78. Herman, I. P. *Physics of the Human Body* (Springer International Publishing, Cham, 2016).
79. Gupta, S., Haiat, G., Laporte, C. & Belanger, P. Effect of the acoustic impedance mismatch at the bone-soft tissue interface as a function of frequency in transcranial ultrasound: a simulation and in vitro experimental study. *IEEE Trans. Ultrason. Ferroelectr. Freq. Control* **68**, 1653–1663 (2021).
80. Jeong, J. Hybrid neural interfacing devices based on Au wires with nanogranular Au shell and hydrogel layer for anti-inflammatory and bi-directional neural communications. *Chem. Eng. J.* **465**, 142966 (2023).
81. Wu, S. et al. Spider-silk-inspired strong and tough hydrogel fibers with anti-freezing and water retention properties. *Nat. Commun.* **15**, 4441 (2024).
82. Wang, H. et al. Super stretchability and satisfactory water retention capacity via a dual-crosslinked hydrogel electrolyte for wide-temperature flexible zinc-air batteries. *Chem. Eng. J.* **498**, 155539 (2024).
83. Wang, Y., Liu, H., Xie, H. & Zhou, S. An autofluorescent hydrogel with water-dependent emission for dehydration-visualizable smart wearable electronics. *Adv. Funct. Mater.* **33**, 2213545 (2023).
84. Nguyen, J. L., Schwartz, J. & Dockery, D. W. The relationship between indoor and outdoor temperature, apparent temperature, relative humidity, and absolute humidity. *Indoor Air* **24**, 103–112 (2014).
85. Domenici, F. Long-term physical evolution of an elastomeric ultrasound contrast microbubble. *J. Colloid Interface Sci.* **540**, 185–196 (2019).
86. Leigh, B. L. et al. Antifouling photograftable zwitterionic coatings on PDMS substrates. *Langmuir* **35**, 1100–1110 (2019).
87. Jung, H., Kim, M. K., Lee, J. Y., Choi, S. W. & Kim, J. Adhesive hydrogel patch with enhanced strength and adhesiveness to skin for transdermal drug delivery. *Adv. Funct. Mater.* **30**, 2004407 (2020).
88. Wang, S. et al. Wearable stretchable dry and self-adhesive strain sensors with conformal contact to skin for high-quality motion monitoring. *Adv. Funct. Mater.* **31**, 2007495 (2021).
89. Zhang, L. et al. Fully organic compliant dry electrodes self-adhesive to skin for long-term motion-robust epidermal biopotential monitoring. *Nat. Commun.* **11**, 4683 (2020).
90. Kim, D.-H. et al. Epidermal electronics. *Science* **333**, 838–843 (2011).
91. Rossetti, A. O. & Laureys, S. *Clinical Neurophysiology in Disorders of Consciousness: Brain Function Monitoring in the ICU and Beyond* (Springer, 2015).
92. Allison, T. et al. Human cortical potentials evoked by stimulation of the median nerve. II. Cytoarchitectonic areas generating short-latency activity. *J. Neurophysiol.* https://doi.org/10.1152/jn.1989.62.3.694.(1989).
93. Buzsáki, G. & Draguhn, A. Neuronal oscillations in cortical networks. *Science* **304**, 1926–1929 (2004).

94. Makeig, S., Debener, S., Onton, J. & Delorme, A. Mining event-related brain dynamics. *Trends Cogn. Sci.* **8**, 204–210 (2004).
95. Yamada, T., Kimura, J., Wilkinson, J. T. & Kayamori, R. Short- and long-latency median somatosensory evoked potentials. Findings in patients with localized neurological lesions. *Arch. Neurol.* **40**, 215–220 (1983).
96. Poornima, S., Ali, S. S., Balaji, P. A., Shankar, V. & Kutty, K. Median nerve somatosensory evoked potentials in medical students: normative data. *Adv. Biomed. Res.* **2**, 56 (2013).
97. Hlushchuk, Y. & Hari, R. Transient suppression of ipsilateral primary somatosensory cortex during tactile finger stimulation. *J. Neurosci.* **26**, 5819–5824 (2006).
98. Lee, W. et al. Transcranial focused ultrasound stimulation of human primary visual cortex. *Sci. Rep.* **6**, 34026 (2016).
99. Lee, W. et al. Image-guided transcranial focused ultrasound stimulates human primary somatosensory cortex. *Sci. Rep.* **5**, 8743 (2015).
100. Duck, F. A. Medical and non-medical protection standards for ultrasound and infrasound. *Prog. Biophys. Mol. Biol.* **93**, 176–191 (2007).
101. Fda, *U. S. Health and Human Services* (Center for Devices and Radiological Health, 2019).
102. Akhtari, M. et al. Somatosensory evoked response source localization using actual cortical surface as the spatial constraint. *Brain Topogr.* **7**, 63–69 (1994).
103. Michel, C. M. & He, B. EEG source localization. *Handb. Clin. Neurol.* **160**, 85–101 (2019).
104. Asadzadeh, S., Yousefi Rezaii, T., Beheshti, S., Delpak, A. & Meshgini, S. A systematic review of EEG source localization techniques and their applications on diagnosis of brain abnormalities. *J. Neurosci. Methods* **339**, 108740 (2020).
105. Koles, Z. J. & Soong, A. C. EEG source localization: implementing the spatio-temporal decomposition approach. *Electroencephalogr. Clin. Neurophysiol.* **107**, 343–352 (1998).
106. Legon, W., Bansal, P., Tyshynsky, R., Ai, L. & Mueller, J. K. Transcranial focused ultrasound neuromodulation of the human primary motor cortex. *Sci. Rep.* **8**, 10007 (2018).
107. Cools, R. & Arnsten, A. F. T. Neuromodulation of prefrontal cortex cognitive function in primates: the powerful roles of monoamines and acetylcholine. *Neuropsychopharmacology* **47**, 309–328 (2022).
108. Yi, S.-S. et al. Ultrasound stimulation of prefrontal cortex improves lipopolysaccharide-induced depressive-like behaviors in mice. *Front. Psychiatry* **13**, 864481 (2022).
109. Sanguinetti, J. L. et al. Transcranial focused ultrasound to the right prefrontal cortex improves mood and alters functional connectivity in humans. *Front. Hum. Neurosci.* **14**, 52 (2020).
110. Folloni, D. et al. Ultrasound modulation of macaque prefrontal cortex selectively alters credit assignment-related activity and behavior. *Sci. Adv.* **7**, eabg7700 (2021).
111. De Ridder, D., De Mulder, G., Verstraeten, E., Sunaert, S. & Moller, A. Somatosensory cortex stimulation for deafferentation pain. *Acta Neurochir. Suppl.* **97**, 67–74 (2007).
112. Strohman, A., Payne, B., In, A., Stebbins, K. & Legon, W. Low-intensity focused ultrasound to the human dorsal anterior cingulate attenuates acute pain perception and autonomic responses. *J. Neurosci.* **44**, e1011232023 (2024).
113. Kim, M. G. et al. Low-intensity transcranial focused ultrasound suppresses pain by modulating pain-processing brain circuits. *Blood* **144**, 1101–1115 (2024).
114. Xia, X. et al. Effects of the motor cortical theta-burst transcranial-focused ultrasound stimulation on the contralateral motor cortex. *J. Physiol.* **602**, 2931–2943 (2024).
115. Heimbuch, I. S. et al. Ultrasound stimulation of the motor cortex during tonic muscle contraction. *PLoS One* **17**, e0267268 (2022).
116. Tang, Y. & Kim, E. S. Simple sacrificial-layer-free microfabrication processes for air-cavity Fresnel acoustic lenses (ACFALs) with improved focusing performance. *Microsyst. Nanoeng.* **8**, 75 (2022).
117. Bhattacharya, S., Datta, A., Berg, J. M. & Gangopadhyay, S. Studies on surface wettability of poly(dimethyl) siloxane (PDMS) and glass under oxygen-plasma treatment and correlation with bond strength. *J. Microelectromech. Syst.* **14**, 590–597 (2005).
118. Lee, B. W., Ryeom, J., Ko, Y. H., Kim, K. J. & Ko, J.-H. Acoustic anisotropy of oriented polyethylene terephthalate films studied through Brillouin light scattering. *J. Soc. Inf. Disp.* **15**, 201–205 (2014).
119. Rossini, P. M., Cracco, R. Q., Cracco, J. B. & House, W. J. Short latency somatosensory evoked potentials to peroneal nerve stimulation: scalp topography and the effect of different frequency filters. *Electroencephalogr. Clin. Neurophysiol.* **52**, 540–552 (1981).
120. Zhang, Z.-G., Yang, J.-L., Chan, S.-C., Luk, K. D.-K. & Hu, Y. Time-frequency component analysis of somatosensory evoked potentials in rats. *Biomed. Eng. Online* **8**, 4 (2009).
121. Wang, Y., Li, G., Luk, K. D. K. & Hu, Y. Component analysis of somatosensory evoked potentials for identifying spinal cord injury location. *Sci. Rep.* **7**, 2351 (2017).
122. Cui, H.-Y., Wu, Y.-X., Li, R., Li, G.-S. & Hu, Y. A translational study of somatosensory evoked potential time-frequency components in rats, goats, and humans. *Neural Regen. Res.* **16**, 2269–2275 (2021).
123. Makeig, S. Auditory event-related dynamics of the EEG spectrum and effects of exposure to tones. *Electroencephalogr. Clin. Neurophysiol.* **86**, 283–293 (1993).
124. Lee, S. & Lee, D. K. What is the proper way to apply the multiple comparison test?. *Korean J. Anesthesiol.* **71**, 353–360 (2018).

Acknowledgements

We thank Wynn Legon, Greg Fonzo, José del R. Millán, Samantha Santacruz and Yaoyao Jia for the discussions and advice. We would like to thank Nanshu Lu for her guidance and providing access to the use of the LPKF Protolaser U4 system. We would like to thank José del R. Millán for providing access to the RehaMove3 FES system. H.W. would like to acknowledge support from Alzheimer's Association New to the Field research grant (AARG-NTF-22-965140), the Department of Defense (DoD) Defense Advanced Research Projects Agency (DARPA) REM-REST grant (HR00112490328), University of Texas at Austin Startup Fund, Texas Proof of Concept (POC) Awards, Cockrell Innovation Grant, National Science Foundation (NSF) CAREER award (2340964) and NIH Maximizing Investigators' Research Award (MIRA) grant (R35GM147408). J.J. would like to acknowledge support from the Human Frontier Science Program (HFSP) fellowship. We acknowledge BioRender.com for the figures drawing.

Author contributions

K.W.K.T., J.J., and H.W. conceived the idea and designed the study. K.W.K.T. led acoustic/electrical characterization of MiniUlTra, acoustic characterization of hydrogel, human tests and their analysis. J.J. led materials characterization of hydrogel and analysis. J-C.H. and M.M.Y. helped with fabrication and mechanical tests of hydrogel. H.D., W.W., X.L., I.P., W.H., W.D.M.B., A.R.L., B.A. assisted in human tests for somatosensory evoked potential suppression. H.H. assisted in laser-etched copper mold for simplified lithographic fabrication of air-cavity Fresnel lens. All the co-authors contributed to the writing of the manuscript. H.W. supervised the project.

Competing interests

The authors K.W.K.T., J.J., J-C.H. and H.W. declare the following competing financial interest(s): A patent application relating to this work has been filed. The remaining authors declare no competing interests.

Additional information

Supplementary information The online version contains supplementary material available at https://doi.org/10.1038/s41467-025-60181-x.

Correspondence and requests for materials should be addressed to Huiliang Wang.

Peer review information *Nature Communications* thanks Christos Papadelis and the other, anonymous, reviewer(s) for their contribution to the peer review of this work. A peer review file is available.